



Originally published as:

Davis, T., Healy, D., Rivalta, E. (2019): Slip on wavy frictional faults: Is the 3rd dimension a sticking point? - *Journal of Structural Geology*, 119, pp. 33—49.

DOI: <http://doi.org/10.1016/j.jsg.2018.11.009>

1 **AUTHORS:**

2 T. DAVIS*^a, D. HEALY^b, E. Rivalta^c

3 ^a davis@gfz-potsdam.de GFZ German Research Centre for Geosciences, Section 2.1: Physics of
4 Earthquakes and Volcanoes. Helmholtzstraße 6/7 Building H 7, Room 201, Potsdam, 14467, Germany.
5 +447914017298.

6 ^b d.healy@abdn.ac.uk School of Geosciences, King's College, University of Aberdeen, Aberdeen, AB24
7 3UE, UK

8 **FUNDING:**

9 T.D. has been funded by the DFG-ICDP, grant agreement N. RI 2782/3-1.

10 **KEYWORDS:**

11 fault; friction; slip; non-planar; opening; corrugated

12 **TITLE:**

13 **Slip on wavy frictional faults: is the 3rd dimension a sticking point?**

14 **ABSTRACT:**

15 The formulation for the 3D triangular displacement discontinuity boundary element method with
16 frictional constraints is described in detail. Its accuracy in comparison to analytical solutions is then
17 quantified. We show how this can be used to approximate stress intensity factors at the crack tips.
18 Using this method, we go on to quantify how slip is reduced on fault surfaces with topography, where
19 the asperities are approximated as a sinusoidal waveform, i.e. corrugations. We use stress boundary
20 conditions (compressive) orientated such that frictional contacts shear. We show that slip reductions
21 relative to planar faults for 2D line and 3D penny-shaped crack models are comparable within 10%
22 when slip is perpendicular to the corrugations. Using the 3D model, we then show how slip is reduced
23 more when corrugation wavelengths are doubled compared to the reduction due to corrugation

24 alignment with the slip direction. When slip is parallel with the corrugation alignment we show that
25 reducing the out-of-plane stress, from the normal traction acting on the fault when planar to that
26 resolved on a perpendicular plane, has the same effect as halving the length of the corrugation
27 waveform in terms of slip reduction for a given amplitude.

28 **1 Introduction**

29 ***1.1 Fault slip profiles***

30 Discontinuities within rock masses such as faults are commonly simplified as broadly planar
31 structures, and relative displacement of the fault faces generates deformation in the surrounding
32 rock. The aim of this paper is to assess the degree to which non-planar fault surfaces influence both
33 the slip (fault parallel) and opening (fault normal) displacements for faults oriented such that they
34 slide in the regional stress field. In the geological literature, an early theoretical treatment of
35 discontinuities in the context of Linear Elastic Fracture Mechanics (LEFM) was outlined by Pollard and
36 Segall (1987). Their text supplies analytical solutions for shearing and opening of the faces of a line
37 crack and the resultant stresses and strains induced in the surrounding material. For these solutions,
38 the medium surrounding the discontinuity is treated as a linear elastic material and the resultant
39 deformation is static, satisfying a uniform stress drop prescribed at the fracture surface. The resultant
40 displacement of the faces is such that these are traction free. Despite the many idealisations, the
41 equations in Pollard and Segall (1987) can be used to gain insight into the slip distribution of faults. A
42 quantitative understanding of fault slip profiles is of interest because:

- 43 • Gradients in slip near the fault tip line are the source of the maximum strains induced by the
44 fault within the wall rock (see the formulas of Pollard and Segall (1987)). These control the
45 location of new fractures or 'damage', which in turn can influence rock strength and
46 permeability;

47 • Fault slip profiles, combined with fault length scaling relationships, can be used to constrain
48 fault displacement on structures where data is sparse (e.g. Kim and Sanderson, 2005), e.g. in
49 the subsurface.

50 • Slip on non-planar faults may promote local opening (or closing) of fault faces, and such
51 movements can impact fault zone permeability, e.g. Figure 4 of Ritz et al. (2015).

52 Numerical models have shown that several parameters can perturb the slip distributions of fault
53 surfaces away from the simple elliptical profiles described in Pollard and Segall (1987). These are:

54 • Fault overlap (Crider, 2001; Kattenhorn and Pollard, 2001).

55 • Fault corrugations (Marshall and Morris, 2012; Ritz and Pollard, 2012; Ritz et al., 2015)

56 • Fault tip-line shape (Willemsse, 1997).

57 • Non-uniform stresses and friction distributions on the fracture surface (Cowie and Scholz,
58 1992; Bürgmann et al., 1994).

59 The focus of this paper is to quantify the effects of non-planar fault surfaces on the slip and opening
60 distributions of isolated faults in three dimensions (3D).

61 **1.2 Motivation: non-planar faults**

62 In this study, we use the term ‘faults’ for surfaces with shear displacement and the term ‘fractures’ or
63 ‘cracks’ more generally for surfaces with low offset where both opening and/or shear displacement is
64 observed, these terms are common in LEFM literature. We focus on metre-scale faults to avoid the
65 additional complexities of gravitational stress gradients, inhomogeneous material interfaces, and
66 damage (Ritz et al., 2015). Several mechanisms cause the faces of fractures in rock masses to deviate
67 from planar, these can occur both during initial fracture growth, and later, as slip accumulates on the
68 fault surface. Examples of such mechanisms are:

69 1. Mixed mode fracture propagation during fracture growth, which introduces relatively
70 cohesionless curved or stepped surfaces into the rock as the fracture tip deviates from a

71 planar path as it grows, this has been shown experimentally (e.g. Thomas and Pollard, 1993;
72 Cooke and Pollard, 1996; Dyskin et al., 2003) and several numerical criteria exist to evaluate
73 this phenomenon (e.g. Erdogan and Sih, 1963; Lazarus et al., 2008; Baydoun and Fries, 2012);
74 2. Fracture growth by linkage of discontinuities, pores, or inclusions (e.g. Olson and Pollard,
75 1989; Janeiro and Einstein, 2010; Huang et al., 2015; Davis et al., 2017);
76 3. Roughening of fault walls during shearing (e.g. Renard et al., 2012, Brodsky et al., 2016).

77 For all these mechanisms parts of the fracture surface will evolve geometrically as it shears. Relative
78 to the final direction of shearing mechanisms 1) and 2) should introduce complex steps in the fracture
79 that have a spread of orientations relative to the direction of shearing, dependent on the boundary
80 conditions driving growth and on the distribution of initial cracks. Assuming the rock is under
81 compression and that the fracture grows by linkage of wing cracks the final fracture will be stepped
82 with steps that are perpendicular to the final direction of shearing (e.g. Yang et al., 2008). For 3)
83 asperities will be aligned parallel with the shear direction. Note the far field stresses driving shearing
84 of the fractures faces can change over time, relative to the alignment of asperities.

85 It is therefore reasonable to question how deviations from a planar surface affect the evolving fault
86 slip profile as a fault shears and slips. In this study, we idealise fault surface roughness as a smoothly
87 and continuously corrugated sinusoidal waveform. Although this is an oversimplification of the
88 roughness of mm-metre scale fault surfaces, it is a useful end member situation for the evaluation of
89 the effects of roughness (and its orientation), on the resultant slip distributions of faults.

90 **1.3 Previous numerical work**

91 The 2D numerical study of Ritz and Pollard (2012) explored how non-planarity affects the resultant
92 slip profiles of fracture surfaces, where non-planarity is modelled as sinusoidal waveforms or
93 'corrugations'. As the study of Ritz and Pollard (2012) is 2D, fracture walls shear perpendicular to the
94 asperities on the fracture faces. The boundary conditions are set such that the two principal stresses
95 driving shearing are both compressive, and the ratio between these is calculated empirically, based

96 on the observations of shearing pre-cut fractures from Byerlee (1978). Ritz and Pollard (2012) showed
97 that as the asperity wavelength decreases, or its amplitude increases, mean slip is reduced. The slip
98 distribution deviates significantly from that of a planar fault.

99 Greater complexity of asperity geometry was introduced in the study of Dieterich and Smith (2009)
100 where fault plane topography was modelled as random fractal roughness. This study also models slip
101 on 2D frictional surfaces and the faults satisfy a uniform shear stress drop aligned with the tips of the
102 fault line. The positive shear stress boundary condition used is equivalent to the stress in a body
103 induced by perpendicular inclined tensional and compressional stress of equal magnitude. This
104 boundary condition puts planes of certain orientations into net tension and is unrealistic for a fault
105 under confining crustal conditions.

106 The 3D numerical analysis of Marshall and Morris (2012) examined the net slip for 3D 'frictionless
107 faults' driven by a uniaxial compressive stress, typically 45° to the fault surface. Constraints were
108 imposed such that the fault faces do not interpenetrate but frictional resistance itself was not
109 considered. The study states that total scalar seismic moment release is not significantly different
110 between rough and planar faults, but this contrasts strongly with the findings of the 2D study of Ritz
111 and Pollard (2012), which has more physically realistic boundary conditions and includes friction.

112 Therefore, we surmise that an analysis in 2D alone cannot provide insights into the mechanics of slip
113 along the corrugation direction. The aim of the current study is to extend the comprehensive 2D
114 analysis of Ritz and Pollard (2012) into 3D. We question how the corrugation orientation in relation to
115 the far field stresses affects slip distributions (including openings) of the fault surfaces. Referring to
116 'in-plane' stresses in our 3D model as those in the plane containing both the faults normal and shear
117 vector direction, we also quantify the effect the 'out-of-plane' stress has on 3D slip distributions.
118 Using similar boundary conditions to Ritz and Pollard (2012), we also quantify the differences
119 between 2D and 3D analyses of such phenomena when corrugations in 3D are also perpendicular to
120 the slip direction.

121 **2 Background**

122 **2.1 Theoretical background and terminology**

123 Figure 1 here

124 As in the study of Pollard and Segall (1987) this study focuses on faults confined within a linear
125 isotropic elastic medium. The material can therefore be described by two elastic constants; here we
126 use Poisson's ratio (ν) and the shear modulus (G). For planar 2D and 3D faults loaded by a constant
127 shear traction as shown in Figure 1, these constants are related to slip in the following manner
128 (Pollard and Segall, 1987; Eshelby, 1963):

$$129 \text{ 2D line crack: } \quad \text{At } L < a, \quad D_s = \frac{(1-\nu)t_s}{G} \sqrt{a^2 - L^2} \quad (1)$$

$$130 \text{ 3D penny-shaped crack: } \text{At } L < a, \quad D_s = \frac{4(1-\nu)at_s}{\pi(2-\nu)G} \sqrt{1 - \frac{L^2}{a^2}} \quad (2)$$

131 Eqs. (1) & (2) supply the displacements (D_s) of the planar cases of a 2D line crack and 3D penny-
132 shaped crack walls loaded by a constant shear traction t_s . Note this is the displacement of one wall of
133 the crack away from its starting position. The result of these equations is that the faces are free of the
134 shear traction imposed due to the resultant slip, note that we ignore tilting of the crack in this study.
135 Here, a is the radius or half-length of the crack and L is the length from the crack centre to an
136 observation point on the crack wall. We use traction in these equations instead of a remote stress
137 driving slip on the crack for two reasons: 1) this removes the dependence on local coordinate systems
138 and relative fracture orientation, and 2) we can directly input friction into these equations without
139 the need for coordinate system transformations. For these equations, both in 2D and 3D, lower values
140 of ν and G cause greater slip of the crack walls. Note that the equations for the opening of a line crack
141 are found by simply replacing t_s by t_n in Eq. (1). For a penny-shaped crack under a tensile stress the
opening displacement and its corresponding stress intensity are found using the line crack equations
for this boundary condition and multiplying these by $2/\pi$.

142 Integrating Eq. (1) and applying shell integration to the radially symmetric curve from Eq. (2) between
 143 the interval 0 to a we can find the total ‘area’ (A) or ‘volume’ (V) of slip of one of the cracks walls. The
 144 results are:

$$2D \text{ line crack: } A = \frac{\pi(1-\nu)t_s a^2}{2G} \quad (3)$$

$$3D \text{ penny-shaped crack: } V = \frac{8(1-\nu)t_s a^3}{3(2-\nu)G} \quad (4)$$

145 Contextually, Eq. (3) is the area under the curve of static slip distributions typically shown for a 2D
 146 fracture, e.g. Ritz et al. (2015). These terms can also be converted to seismic moment using Eq. (5):

$$M_0 = V * G \quad (5)$$

147 Faults buried in the subsurface will be subject to a non-zero confining stress, depending on depth. A
 148 proportion of this force resolves as a compressive force directed along the surfaces normal; resolving
 149 the force as a traction we adopt the notation t_n . The normal and shear tractions on the surface can be
 150 combined with friction to find the resolved shear traction driving slip on the fault surface (Pollard and
 151 Fletcher, 2005):

$$|t_{s_res}| = |t_s| + \mu t_n - S_f \quad (6)$$

152 The result of Eq. (6) can be put into Eqs. (1) – (4) to find the slip profile of a fault under crustal stress
 153 conditions. Eq. (6) describes the resultant shear traction t_{s_res} on a plane under compression after the
 154 frictional properties, the coefficient of friction (μ) and cohesion (S_f), have been considered. The bars
 155 surrounding t_s represent the use of absolute values. We adopt a convention where a negative value in
 156 t_n represents a compressive force. Note that Eq. (6) ignores the sign and therefore the relative
 157 direction of the input t_s .

158 **2.2 Motivation**

159 Visual examples of fault roughness show it is ubiquitous but varied e.g. (Cann et al., 1997; Sagy &
 160 Brodsky, 2007; Jones et al., 2009; Griffith et al., 2010; Ritz et al., 2015). Many previous studies of
 161 rough fault surfaces have focussed on the scaling of roughness (Resor and Meer, 2009; Candela et al.,

162 2011). Other studies look at how such corrugations deflect slip, at both kilometre fault scales (Roberts
163 and Ganas, 2000) and locally on the fault surface (Kirkpatrick and Brodksy, 2014). Recent
164 experimental studies have attempted to model how friction changes with the contact area and
165 development of asperities and shear surfaces (e.g., Harbord et al., 2017). The aim of such studies is to
166 look at how roughness and pressure change the contact area of the asperities and hence the friction.
167 Fracture geometry and roughness also influences fracture stiffness and has been shown
168 experimentally to control nucleation points of slip surface displacement (Choi et al., 2014; Hedayat et
169 al., 2014).

170 Although much of the previous work on rough faults has centred on the roughness itself and the
171 scaling, there has been less work on the mechanics of rough faults, especially in 3D. In this study, a
172 single-scale ‘roughness’ wavelength is used in each model. This neglects roughness below a certain
173 scale, assuming that small-scale asperities and their contact mechanics can be reduced to the
174 mechanical problem of a planar surface with a uniform coefficient of friction, which is the underlying
175 assumption of Coulomb’s friction law (Persson, 2006). This study therefore focuses on how the larger
176 scale geometrical asperities of a surface, in relation to both the remote stresses and the shearing over
177 these irregularities, inhibits or promotes the sliding of faults.

178 **3 Displacement discontinuity method with friction**

179 In this section, we detail the numerical method used to model sliding surfaces with frictional
180 properties. A frictional adaptation of the displacement discontinuity boundary element method
181 (DDM) is employed. Such adaptations in 3D have been described in previous works (Kaven et al.,
182 2012). For the sake of clarity in notation and in defining a clear convention we describe the matrix
183 system here.

184 3.1 3D DDM formulation: equations, elements and convention

185 The whole space triangular element formulations of Nikkhoo and Walter (2015) are used as the basic
 186 displacement discontinuities in our method. The elements in this publication describe the stress
 187 perturbations and displacements in an isotropic linear elastic medium caused by the face of a planar
 188 triangle displacing with a constant mirrored movement. In the method, boundaries are meshed as 3D
 189 triangulated surfaces, where each face of the mesh acts as a triangular dislocation. Coefficient
 190 matrices $[A]$ are built and a vector is supplied that describes the remote stresses resolved as a traction
 191 $[t^\infty]$ at each face of the boundary. The displacement discontinuity method in 3D is then solved as:

$$D = -A^{-1}t^\infty \quad (7)$$

192 Expanding Eq. (7) for the 3D DDM method the matrix system is as follows:

$$\begin{bmatrix} D_n^i \\ D_{ss}^i \\ D_{ds}^i \end{bmatrix} = - \begin{bmatrix} A_{D_n t_n}^{ij} & A_{D_{ss} t_n}^{ij} & A_{D_{ds} t_n}^{ij} \\ A_{D_n t_{ss}}^{ij} & A_{D_{ss} t_{ss}}^{ij} & A_{D_{ds} t_{ss}}^{ij} \\ A_{D_n t_{ds}}^{ij} & A_{D_{ss} t_{ds}}^{ij} & A_{D_{ds} t_{ds}}^{ij} \end{bmatrix}^{-1} \begin{bmatrix} t_n^i \\ t_{ss}^i \\ t_{ds}^i \end{bmatrix} \quad (8)$$

193 In this system, D is a vector containing the movement of each triangles face (i.e. a displacement
 194 discontinuity), where subscripts n , ds and ss represent displacement of the faces in the normal, dip-
 195 slip, and strike-slip directions respectively. Vector t^∞ represents the remote stress resolved as a
 196 traction on the mid-points (geometric incenter) of each triangular face. The sign of A is flipped as we
 197 have adopted the same sign convention for the displacement of discontinuities and direction of
 198 traction, summarised in Figure 2.

199 **Figure 2 here**

200 For each sub-matrix of square coefficient matrix A in Eqs. (7) & (8), the first subscript D represents
 201 the displacement of an element with its direction defined by the lower subscripts. The second
 202 subscript t represents the traction in the direction of its respective subscript. For example, $A_{D_n t_{ss}}^{ij}$ is a
 203 square matrix that describes how much an opening displacement of one unit length at element j

204 effects the strike-slip shear traction on element i . Each column in this matrix is the effect of one
 205 element on the mid-point of every other element.

206 **3.2 Aims of the DDM solution**

207 In Eqs. (7) & (8), the aim is to find a static slip distribution that approximates the mid-point of each
 208 face of the boundary as traction free (t_n & t_{ss} & $t_{ds} = 0$) under the given remote stress defined in the
 209 vector t^∞ on the right-hand side of the equation. Once D is found, DA results in traction vector t^B ,
 210 which represents the stresses at each mid-point induced by the displacement of the cracks walls. The
 211 result of Eq. (7) is that t^B and t^∞ should oppose each other resulting in a solution where there is no
 212 traction at any triangle mid-point along the meshed boundary (Eq. (9)).

$$0 = t_n^B + t_n^\infty \tag{9}$$

$$0 = t_{ss}^B + t_{ss}^\infty$$

$$0 = t_{ds}^B + t_{ds}^\infty$$

213 **3.3 DDM formulation with friction**

214 To add frictional constraints to this problem, the system of equations (7) & (8) is reformulated as a
 215 linear complementarity problem (Kaven et al., 2012). We use the open source complementarity solver
 216 of Niebe and Erleben (2015) implemented in MATLAB. For full details on the accuracy and
 217 convergence criterion of the complementarity solver see Niebe and Erleben (2015). For our analysis
 218 we have used the default converge criterion of 10 times the numerical precision and the zero Newton
 219 equation strategy supplied in the code. Following the notation of Niebe and Erleben (2015) the linear
 220 complementarity problem can be stated as:

$$y = ax + b \tag{10}$$

221 In Eq. (10) x , y , and b are vectors and a is a square matrix. For this problem, the following constraints
 222 are set:

$$x \cdot y = 0 \quad (11)$$

$$y \geq 0 \quad (12)$$

$$x \geq 0 \quad (13)$$

223 In this formulation vectors x and y are unknowns representing tractions and or displacement
 224 discontinuities as the solver progresses. They are created such that each pair of corresponding values
 225 in the vectors contains a traction and displacement discontinuity and that the sign convention in
 226 vector x is flipped. Vector b is filled with the results from Eq. (8), if all displacements are positive
 227 according to our convention all constraints are already met, D_n must be positive so the coefficient of
 228 friction does not need to be considered. If any displacements in b are negative, then the constraint in
 229 Eq. (12) is not met and x will begin to fill with opposing with non-zero values. The expanded form of
 230 Eq. (10) for a 3D DDM problem is:

$$\begin{bmatrix} DF_n^{i+} \\ DF_{ss}^{i+} \\ DF_{ds}^{i+} \\ t_{ss}^{i+} \\ t_{ds}^{i+} \end{bmatrix} \quad (14)$$

$$= \begin{bmatrix} (C_{D_n t_n}^{ij} - (C_{D_n t_{ss}}^{ij} * I\mu^i) - (C_{D_n t_{ds}}^{ij} * I\mu^i)) & C_{D_n t_{ss}}^{ij} & C_{D_n t_{ds}}^{ij} & 0 & 0 \\ (C_{D_{ss} t_n}^{ij} - (C_{D_{ss} t_{ss}}^{ij} * I\mu^i) - (C_{D_{ss} t_{ds}}^{ij} * I\mu^i)) & C_{D_{ss} t_{ss}}^{ij} & C_{D_{ss} t_{ds}}^{ij} & I & 0 \\ (C_{D_{ds} t_n}^{ij} - (C_{D_{ds} t_{ss}}^{ij} * I\mu^i) - (C_{D_{ds} t_{ds}}^{ij} * I\mu^i)) & C_{D_{ds} t_{ss}}^{ij} & C_{D_{ds} t_{ds}}^{ij} & 0 & I \\ 2 * I\mu^i & -I & 0 & 0 & 0 \\ 2 * I\mu^i & 0 & -I & 0 & 0 \end{bmatrix} \begin{bmatrix} t_n^{i-} \\ t_{ss}^{i-} \\ t_{ds}^{i-} \\ DF_{ss}^{i-} \\ DF_{ds}^{i-} \end{bmatrix}$$

$$+ \begin{bmatrix} D_n^{i+} - (C_{D_n t_{ss}}^{ij} * S_f^i) - (C_{D_n t_{ds}}^{ij} * S_f^i) \\ D_{ss}^{i+} - (C_{D_{ss} t_{ss}}^{ij} * S_f^i) - (C_{D_{ss} t_{ds}}^{ij} * S_f^i) \\ D_{ds}^{i+} - (C_{D_{ds} t_{ss}}^{ij} * S_f^i) - (C_{D_{ds} t_{ds}}^{ij} * S_f^i) \\ 2S_f^i \\ 2S_f^i \end{bmatrix}$$

231 Where:

$$\begin{bmatrix} C_{D_n t_n}^{ij} & C_{D_n t_{ss}}^{ij} & C_{D_n t_{ds}}^{ij} \\ C_{D_{ss} t_n}^{ij} & C_{D_{ss} t_{ss}}^{ij} & C_{D_{ss} t_{ds}}^{ij} \\ C_{D_{ds} t_n}^{ij} & C_{D_{ds} t_{ss}}^{ij} & C_{D_{ds} t_{ds}}^{ij} \end{bmatrix} = - \begin{bmatrix} A_{D_n t_n}^{ij} & A_{D_{ss} t_n}^{ij} & A_{D_{ds} t_n}^{ij} \\ A_{D_n t_{ss}}^{ij} & A_{D_{ss} t_{ss}}^{ij} & A_{D_{ds} t_{ss}}^{ij} \\ A_{D_n t_{ds}}^{ij} & A_{D_{ss} t_{ds}}^{ij} & A_{D_{ds} t_{ds}}^{ij} \end{bmatrix}^{-1} \quad (15)$$

232 Eq. (14) describes the 3D complementarity equation system for friction on fault surfaces in the 3D
 233 DDM method. C is the matrix inverse of the collated coefficient matrix A from Eq. (8); the sub-
 234 matrices of C are extracted as in Eq. (15). Matrix C can be described as follows: the summed influence
 235 of all elements displacing the amount described in each column of matrix C will cause a traction of
 236 one stress unit, t^B on element (i) in the direction defined by the subscript. The other traction
 237 components at this element and all tractions at every other element will be 0. S_f (the cohesive
 238 strength of the material) and μ (the coefficient of friction) are defined as vectors, with one value for
 239 each element. I is an identity matrix (a square matrix of zeros with ones on the main-diagonal). DF
 240 represents the resultant displacement discontinuities when friction is considered. Values of D in
 241 vector b (Eq. (14)) are the results of Eq. (8). Negative superscripts in Eq. (14) (vector x) are values with
 242 the opposite sign to the convention shown in Figure 2. This means that once solved, positive values in
 243 x of Eqs. (10) & (14) must be flipped in sign so the boundary displacements cause stresses that satisfy
 244 Eq. (9). The resultant displacement discontinuities at each face are therefore calculated from the
 245 results of Eq. (10) as:

$$D = y - x \quad (16)$$

246 Note, this assumes that the corresponding vectors from x and y are extracted and aligned before this
 247 is performed.

248 To stabilise the implementation, matrix conditioning is used. The matrix A in Eq. (15) is scaled by a
 249 constant before it is inverted. This constant is the mean value of the half-perimeter length of all the
 250 triangles divided by the shear modulus. In the 2D code for line elements we use a similar scaling, the
 251 mean element half-length divided by the shear modulus, multiplied by 100. The output element
 252 displacements of Eq. (14) are simply multiplied by this scalar value to find the true displacements.

253 Without this scaling, the solver may fail to converge if both the coordinates and/or driving stresses
254 are not scaled around values close to one. Note that the scaling described here assumes that the
255 elements in the model have similar length scales and shapes.

256 **3.4 Aims of the frictional DDM solution**

257 Eqs. (10) & (14) attempt to reach a solution where all elements are free of t_{s_res} , which is the shear
258 traction calculated using Eq. (6), either through shearing or opening of elements. Note that each
259 element only shears if its frictional constraints allow it. The resultant boundary should also be free of
260 tensile tractions defined in vector t^∞ . This solution explicitly factors in changes in the normal or shear
261 traction and the associated frictional resistance due to the displacement of elements in the result as
262 the solver progresses. In the formulation described, the input mesh represents an infinitesimally thin
263 crack with initially coincident faces. To allow given surfaces to interpenetrate in this formulation an
264 arbitrarily large value bigger than the amount needed to close the fracture in the stress field can be
265 added to D_n for the necessary elements vector b in Eq. (10)/(14). This value is then subtracted from
266 these elements in the outputs of Eq. (16). An example use case is modelling both fractures and
267 stresses due to topographic loading, such topographic stresses can be modelled with the BEM as
268 described in Martel and Muller (2000) where elements representing the topography must be able to
269 both open and close. This manipulation also allows for the modelling of initially open fractures, the
270 value added to the vector b in this case would be the fractures initial opening profile.

271 **Figure 3 here**

272 Figure 3 shows the polygonal frictional approximation as described in Kaven et al. (2012). Figure 3a)
273 shows a cross section through the 3D friction cone; in 2D this takes a form comparable to the typical
274 failure envelope of a Mohr-Coulomb plot. Both points P and Q are the same distance in y from the
275 grey cone, therefore have the same resultant traction driving shearing. Figure 3b) shows a) extended
276 to 3D space. In 3D space, the pyramidal approximation is shown by the dotted lines. In this numerical

277 approximation, the elements with shear tractions large enough to plot outside of the ‘pyramid’ will
278 displace, rather than those that plot inside the cone. Figure 3c) shows an end-on view of the cone
279 shown in b). The approximation overestimates friction for any part of vector t_s that passes through
280 the dark grey area between the pyramidal approximation (square) and the isotropic friction cone
281 (circle). It is clear that this is highest at faces where t_{ds} and t_{ss} are equal. For this situation friction is
282 overestimated by 41% (Kaven et al., 2012).

283 **4 Benchmarking and model setup**

284 ***4.1 Boundary conditions and shear profile of the crack***

285 This test of the numerical method uses the same boundary conditions, initial geometry, and sampling
286 as the remainder of the analysis in this study.

287 **Figure 4 here**

288 **Figure 5 here**

289 Figure 4 is a comparison of the numerical result to the slip profile of a penny-shaped crack as
290 described by Eq. (2). The geometry of the problem is shown in Figure 5. The stress convention used
291 puts σ_1 as the least compressive stress. The boundary conditions have been chosen such that in the
292 xy -plane these match the empirically defined boundary conditions of Ritz and Pollard (2012).

293 Here we summarise the motivation behind the chosen boundary conditions in Ritz and Pollard (2012),
294 Byerlee (1978) finds that the maximum friction of rocks in the upper crust (normal stress of up to
295 200MPa) occurs when $0.85t_n = t_s$. Maximum friction being the point in experiments when the contact
296 between two separate blocks of material suddenly shears. Using the ratio 0.85 as the coefficient of
297 friction and placing Eq. 9.45 into Eq. 6.55 of Pollard and Fletcher (2005) as the value of a_x and
298 rearranging to find the ratio between σ_{xx} and σ_{yy} (treating these as principal stresses by ignoring σ_{xy})
299 the following equation is found:

$$\frac{\sigma_3}{\sigma_1} = 2 \frac{t_s}{t_n} \sqrt{\left(\frac{t_s}{t_n}\right)^2 + 1} + 2 \left(\frac{t_s}{t_n}\right)^2 + 1 \quad (17)$$

300 For a ratio of t_n to t_s of 0.85 this results in a principal stress ratio of 4.68, Eq. 9.45 of Pollard and
 301 Fletcher (2005) supplies the angle of these principal stresses away from the fracture plane, 24.8° . The
 302 friction coefficient of the fractures face in our model is set to a value less than 0.85, this takes the
 303 fracture surface past failure, allowing it to slip in the defined stress field. We orientate the 3D surface
 304 so that its normal points along the y -axis, i.e. an extension of a 2D model. Here θ is set at 24.8° and is
 305 the angle of the normal away from σ_3 . The results supplied in the rest of the analysis are scaled
 306 relative to these analytical solutions so are dimensionless and can be scaled as necessary.

307 For the modelling the following parameters were used: the fault radius (a) was set to 1 metre and σ_1
 308 and σ_3 were set to -50 MPa and -233.8 MPa respectively, adhering to the ratio defined above. When
 309 resolved into Cartesian tensor components with the fault plane oriented as above these are: $\sigma_{xx} = -$
 310 201.5 MPa, $\sigma_{yy} = -82.3$ MPa and $\sigma_{xy} = -70.0$ MPa. The shear modulus (G) was set at 12 GPa while the
 311 Poisson's ratio (ν) was set to 0.25. The frictional properties were as follows: no cohesive strength was
 312 imposed and the dimensionless value of μ was set to 0.6 (Pollard and Fletcher, 2005; Harbord et al.,
 313 2017). For these parameters, the maximum slip from Eq. (2) scales with fracture length ($2a$) in a
 314 1:1,000 relationship. Such a scaling lies at the lower end of shear fractures observed in the field (Kim
 315 and Sanderson, 2005).

316 The analytical solution from Eq. (2) is plotted on Figure 4 with the boundary conditions stated above
 317 driving slip. The surface is meshed using a grid of points within a circle on the xz -plane that have a
 318 spacing of 1/65 m. Points on this grid 0.02 m from the circles edge were removed and equilateral
 319 triangles were added to approximate a smooth outer boundary of the crack, see Figure 17. The
 320 overestimation of the crack shear displacement at the tip region of the fracture is $30\% \pm 5\%$ as shown
 321 in Figure 4. Note that the angular dependency of error is dependent on the mesh used.

322 In the subsequent analysis, we plot the relative area (or volume) of slip on the fault surface to indicate
 323 how it is reduced by the fault geometry. This can be calculated numerically with the 2D and 3D DDM
 324 using:

$$2D \quad A = \frac{\sum(D_s * 2a)}{\sum(2a)} \quad (18)$$

$$3D \quad V = \frac{\sum(D_s * T)}{\sum T} \quad (19)$$

325 Where A and V are the area and volume of slip of the 2D or 3D fracture, respectively. T in Eq. (19) is
 326 the area of each triangles face and a is the half-length of the 2D elements. D_s is the shear
 327 displacement calculated at each element. The following equation is used to evaluate the slip decrease
 328 on wavy faults from the reference slip observed for a planar penny-shaped crack:

$$\% A \text{ reduction} = [100/A_p] * [A_p - A_w] \quad (20)$$

$$\% V \text{ reduction} = [100/V_p] * [V_p - V_w] \quad (21)$$

329 **Figure 6 here**

330 where the subscript p is the slip of a planar fault, i.e. Eq. (3) & (4) and the subscript w that of a wavy
 331 fault. Figure 6 shows diagrammatically the slip distribution for a planar and a wavy fault. Eq. (21) here
 332 would describe the volume between the planar and wavy surfaces.

333 A second test of the accuracy of the numerical setup in 3D is to calculate how well Eq. (19)
 334 approximates Eq. (4) when the fault is planar. Using Eq. (21) this results in a value of 1.08%. The error
 335 is deemed acceptable for the current analysis as our results look at levels of slip reduction greater
 336 than 1%. This gives an insight into the numerical accuracy of results shown later, where the sampling
 337 in 3D described above is used. We have also run our 3D analysis for a mesh as described previously
 338 but with half the number of triangles to test how sensitive our results are to sampling. Comparing for
 339 the waveform where the observed change in volume and stress intensity reductions is steepest ($H =$
 340 1% of a and $\lambda = 25\%$) we see a maximum difference of 1.5% for the stress intensity and volume of slip

341 reductions reported in our results (Figure 8 to Figure 12). Our mesh sampling is therefore deemed
 342 high enough to provide stable results at the scales of reduction in these properties that we report.
 343 Our last test of accuracy is to use the output slips from Eq. (16) and compute the tractions using Eq.
 344 (8). Converting the boundary conditions to tractions and using Eq. (6) we find the analytical resultant
 345 traction. Comparing the analytical and numerical tractions at every elements midpoint, the highest
 346 error observed is 1E-7% of the analytical value. This is deemed sufficiently accurate in capturing the
 347 boundary condition set.

348 Corrugations were introduced onto the surface using Eq. (22). The resultant undulations are aligned
 349 along the z -axis created by moving each triangles corner point by the y value of the prescribed
 350 waveform. To orient these corrugations at different angles to the slip sense a rotation of the surface
 351 around the y -axis was then applied (Figure 5b to c).

$$y = H \sin\left(\frac{2\pi x}{\lambda}\right) \quad (22)$$

352 Where H is the waveform amplitude and λ the wavelength. Note that we have set an upper limit to
 353 the waveforms used in this analysis such that the inflection points on the waveforms (where $y = 0$)
 354 are never angled more than 45 degrees away from the x -axis.

355 **4.2 Stress intensity approximation**

356 Stress intensity factors approximate stress distributions and magnitudes at distances very close to a
 357 fracture's tip. For a 2D fracture (shear or opening) these have been shown to approximate stress
 358 distributions at distances of 10% of the fractures half-length from the tip with less than 15% error
 359 (Pollard and Segall, 1987; Pollard and Fletcher, 2005). The accuracy of this approximation increases
 360 with decreasing distance from the fracture's tip. In 2D the formula for the stress intensity of a line
 361 crack subjected to shearing is:

$$2D \text{ line: } K_{II} = t_s \sqrt{a/\pi} \quad (23)$$

362 Following Tada et al. (1973) the formulas for the stress intensity factors around a penny-shaped crack
 363 subject to shearing are:

$$\begin{Bmatrix} K_{II} \\ K_{III} \end{Bmatrix} = \begin{Bmatrix} \cos \theta \\ \sin \theta (1 - \nu) \end{Bmatrix} \frac{4t_s \sqrt{a/\pi}}{2 - \nu} \quad (24)$$

364 Where θ is measured from the crack centre and defines the angle between the shear direction and a
 365 location on the crack's tip-line, (Figure 1). The results of the DDM method can be used to approximate
 366 the stress intensity factors at a fracture's tip (Olson, 1991). We have followed the method of Olson,
 367 (1991) but re-derived the formulas using the equations for a 3D penny-shaped crack (Appendix A).
 368 The 3D formulas are:

$$\begin{Bmatrix} K_I \\ K_{II} \\ K_{III} \end{Bmatrix} = \begin{Bmatrix} D_n \\ D_{II} \\ D_{III}(1 - \nu) \end{Bmatrix} \frac{\sqrt{\pi}G}{\sqrt{h}(1 - \nu)^2} c \quad (25)$$

369 In these equations, h is the distance from the mid-point (geometric incenter) of the boundary
 370 element to the fracture's tip (Ritz et al., 2012), D_n is the normal displacement of this element, D_{II} is
 371 the displacement perpendicular to the crack edge, and D_{III} is the displacement parallel with the edge.
 372 The correction factor c is used to correct for the errors due to the numerical approximation. This is set
 373 to 1/1.834. See the appendix for the reasoning.

374 **Figure 7 here**

375 The accuracy of the 3D DDM in matching Eq. (24) is shown in Figure 7. The maximum vertical
 376 separation between the analytical curve and points (residual) shown in Figure 7 is 0.032 for K_{II} and
 377 0.035 for K_{III} , this is for the surface as described in Section 4.1.

378 **5 Model results**

379 **5.1 Effect of corrugation amplitude and wavelength: comparison to 2D results**

380 We now compare the slip reduction differences for 2D and 3D geometries with the same shaped
 381 corrugations. The results of Eqs. (20) & (21) are plotted to compare the slip area or volume reduction

382 relative to a planar fault. The fault in 3D is oriented as in Figure 5b. For this configuration, the ‘out-of-
383 plane stress’ σ_{zz} in 3D makes no difference to the results as this is not resolved as a traction at any
384 point on the surface.

385 **Figure 8 here**

386 Figure 8 shows a comparison between the results for 2D and 3D wavy faults with several amplitudes
387 and four different wavelengths. The 2D sampling has been set to 1,000 equally spaced elements on
388 the fault plane in the x -axis before the waveform is introduced. Slip reductions relative to a planar
389 penny-shaped and line cracks are plotted in Figure 8 as a function of the surface waveform, and both
390 2D and 3D results are shown. This shows the simple trends observed in previous 2D studies where
391 resultant slip is reduced by corrugations with higher amplitudes and/or shorter wavelengths (Ritz and
392 Pollard, 2012).

393 Trends, due to both changes in amplitude (H) and wavelength (λ), in the reduction in slip are similar
394 for the 2D and 3D results. The largest difference between 2D and 3D reductions in slip due to
395 corrugations is less than 10%. Some notable differences are that the 2D results have greater
396 reductions in slip for all modelled wavelengths, except for when the wavelength is larger than the
397 fault half-length (in this case the opposite is true). As the numerical accuracy of the DDM has been
398 quantified as accurate to approximately 1%, the difference between the two results is due to the
399 shape and area of the crack in 3D and the lack of the plane strain boundary condition. From these
400 results, we suggest that the slip distribution profiles documented by Ritz and Pollard (2012) for 2D
401 fractures can be extrapolated to 3D penny-shaped fractures when shearing is perpendicular to the
402 alignment of asperities.

403 **5.2 Effect of corrugation orientation in 3D**

404 In this section, we explore the effects of corrugation orientation in relation to the direction of
405 shearing, i.e. changing from the geometry shown in Figure 5b to that in Figure 5c. When corrugations

406 are oriented as in Figure 5c this means σ_{zz} is resolved as a normal traction on some parts of the
407 surface. We start by exploring the changes in slip volume when σ_{zz} is set to the same magnitude as
408 the stress component, σ_{xx} ; this is t_n acting on the plane if it was perpendicular to its orientation shown
409 in Figure 5a. Changes in the magnitude of σ_{zz} are explored later.

410 Figure 9 is an example that shows the shearing of a faults faces for the geometries in Figure 5b and
411 Figure 5c. An important observation from this figure is that there is no slip in the z direction. The lines
412 running parallel with the x-axis are not perturbed. This is different to the findings of Marshall and
413 Morris (2012) where deviations in slip vector rake are analysed on frictionless faults. For high values
414 of friction and for these boundary conditions the fault plane only slips in directions parallel to the
415 greatest resolved shear traction vector.

416 **Figure 9 here**

417 **Figure 10 here**

418 Figure 10 has the same axes and plots the same corrugation waveforms as Figure 8 but compares slip
419 reductions when corrugations are parallel and perpendicular to the slip direction (Figure 5b to c).

420 Reviewing the trends in this graph shows that:

- 421 • The range in slip reduction due to doubling the wavelengths of corrugations (vertical distance
422 between lines with the same symbol) is almost always greater than the reduction due to
423 corrugation misalignment for a given corrugation waveform (vertical extent of each shaded
424 patch).
- 425 • Faults with shorter corrugation wavelengths are more sensitive to corrugation angle relative
426 to slip. These have greater ranges in slip as the corrugation directions change from parallel to
427 perpendicular in relation to the plane containing the most compressive stress.

428 **Figure 11 here**

429 Figure 11 explores what the out-of-plane stress (here σ_{zz}) does to the results of Figure 10. Two cases
430 are shown: a) σ_{zz} is set equal to σ_{xx} ; b) σ_{zz} is equal to σ_{yy} (i.e. t_n when planar). The figure shows slip
431 reductions when corrugations are parallel with the slip direction. For cases when σ_{zz} is reduced so is
432 the additional frictional resistance which allows the fault to slip a greater amount. Here it can be seen
433 that doubling the wavelength of the corrugations (vertical distance between lines with the same
434 symbol) has close to the same effect in reducing slip as decreasing the out-of-plane stress σ_{zz} to the
435 magnitude of the lowest stress driving slip (vertical extent of each shaded patch).

436 Adjusted coefficients of friction are supplied for planar faults in Figure 11 to give an idea of how this
437 parameter reduces slip volume in comparison to the reductions due to fault waveform. Note these
438 values also apply to Figure 8 and Figure 10 also. This gives some idea of the 'effective' friction that
439 would be calculated by fitting a planar fault model to slip data from a wavy fault surface that was
440 subject to the boundary conditions we have described.

441 **5.3 Stress intensity factors**

442 Reductions in stress intensity between the 2D and 3D results are shown in Figure 12. This figure plots
443 results relative to the result from Eq. (24). Note that the 3D results plot the maximum stress intensity
444 on the crack edge. Unlike in Figure 8 the trends between 2D and 3D results are quite disparate, <40%
445 in places. This is due to the crack tip in 2D being a single point. Figure 9 shows that parts of the fault
446 surface slip less due to the waveform of the fault surface and its relation to the principal stresses. In
447 2D if the crack tip is at a location where the slip is reduced then so is the stress intensity. In 3D, the
448 crack has a tip-line so even if slip along parts of its tip-line are reduced, locations along parts of the
449 tip-line in 'releasing bends' will continue to slip. This results in some edges of the fault maintaining
450 higher stress intensities. Note that reductions in K_{III} for the 3D case follow very similar trends to that
451 of K_{II} . This observation highlights the need for careful consideration of geometry and local departures

452 from the general trends when analysing the results of the previous graphs, Figure 8, Figure 10, and
453 Figure 11.

454 **5.4 Effect of waveform on opening aperture**

455 This part of the study focuses on the ‘lenticular’ openings as described by Ritz et al. (2015). The same
456 basic boundary conditions and constants are used as before, but with an additional pore pressure
457 inside the fracture. In this part of the study a 2D plane strain code is used to model slip perpendicular
458 to the asperity direction. In the 2D study of Ritz and Pollard (2012) a ratio a/λ greater than 11 (when λ
459 is less than ~9% of a) was required before opening was observed on parts of the fractures face. We
460 look at openings for faults with longer corrugation wavelengths when there is a pore pressure (P)
461 acting to reduce the effective normal stress confining the surface. From Eq. (6) we can state that
462 increases in pore pressure should increase the overall slip on the fracture surface, this should also
463 promote opening of the surfaces faces:

$$2D \text{ line: At } L < a, \quad D_n = \frac{2(1-\nu)P}{G} \sqrt{a^2 - L^2} \quad (26)$$

464 We choose to scale the maximum apertures observed on the wavy faults, so they are relative to the
465 maximum opening observed for a planar line shaped crack dilating due to an internal pressure, (Eq.
466 (26)). D_n here being the total separation between the faces not just the displacements of one wall of
467 the crack. Note that the maximum opening here is found by simply setting the term L inside the
468 square root to zero, i.e. the centre of the crack (Figure 1). This allows us to scale our results to a
469 problem that uses both the same elastic constants and has the same surface geometry (when planar)
470 making our results dimensionless. The internal pressure opening the crack is set to half the magnitude
471 of the normal stress that confines our shear fault when it is planar. In terms of pressure this is a value
472 P , 41.15 MPa.

473 **Figure 13 here**

474 Figure 13 shows how openings on the fracture surface change as a function of the waveform of the
475 fracture. The two axes show the parameters that control the waveform and the coloured squares are
476 openings as a percentage of Eq. (26). Note that the dashed lines shown are where waveform slopes
477 are deemed excessive (see Section 4.1). The graph shows that lenticular openings on confined shear
478 fractures can reach up to 25% of the maximum apertures of an unconfined pressurised crack.
479 Maximal openings are found for waveforms with ratios of λ/H of around 15. Such a ratio and the
480 opening magnitudes will change with friction, pore pressure and driving stresses.

481 **6 Discussion**

482 **6.1 Relationships in slip reduction**

483 From the modelling results, the following statements can be made:

- 484 1. When slip is perpendicular to the corrugations, results from 2D studies match closely with 3D
485 results (Figure 8). This suggests that the slip reductions due to the shape of corrugations are
486 not greatly affected by the tip-line shape of the fracture so plane strain (2D) modelling is
487 adequate in this case.
- 488 2. When slip is parallel to corrugations, reductions due to doubling corrugation wavelength are
489 greater than the slip reduction due to rotation of the corrugations out of alignment with the
490 slip direction (Figure 10). This is provided that the out-of-plane stress is high, high being the
491 value of t_n resolved on the crack face when planar.
- 492 3. For slip parallel with corrugations, the maximum reduction in slip when changing the out-of-
493 plane stress from low to high matches the reduction in slip when halving the corrugation
494 wavelength. Low here being the value of t_n resolved on a planar crack orientated
495 perpendicular to the crack in our setup (with its normal in the xy -plane).

496 These results should give some indication as to which fault shapes will preferentially accrue more slip
497 in a given slip direction. Such results rely on both an estimation of fault roughness at a larger scale

498 and the stresses driving failure. Note the two latter relationships detailed here are dependent on the
499 coefficient of friction being at 0.6. We have tested if these statements hold true for values of μ
500 between 0.4 – 0.67. Statements 1 and 3 hold true between these values. Statement 2 is still valid
501 when μ is higher, i.e. 0.67, but begins to break down for lower values i.e. 0.4. Here results for the
502 different wavelengths would begin to overlap in Figure 10.

503 It is worth reviewing the statements earlier that friction is overestimated by 41% on faces where the
504 two shear traction components (t_{ds} and t_{ss}) are of equal magnitude. We can therefore state that
505 trends for the slip parallel with corrugations in Figure 10 and Figure 11 will show greater reductions
506 due to friction than would be observed if we modelled this using an isotropic friction cone.

507 **6.2 Additional complexity**

508 In 2D the correlation between slip reduction and stress intensity is clear; see Figure 8 and Figure 12.
509 This breaks down in 3D where high stress intensities remain even when the total volume of slip is
510 significantly reduced. Similar examples of local departures from the global trend of slip on the fault
511 surface were presented by Ritz and Pollard (2012); here we have shown an example where 3D
512 geometry also introduces such a complexity.

513 Changing the start location and sign of the waveform (phase shift) for faults with longer corrugation
514 wavelengths changes the slip distributions (Ritz and Pollard 2012). Changing these parameters will
515 only have substantial effects on slip reductions for corrugations of longer wavelengths, for example
516 the greatest slip reduction shown for the longest wavelength in Figure 8 increases by up to 10% for a
517 waveform shifted positively by 90 degrees. The other wavelengths modelled here are broadly
518 unaffected (less than 5%).

519 **Figure 14 here**

520 An obvious question related to the results shown here is how well does the approximation of a
521 smoothly undulating roughness compare to slip on surfaces with real fracture surface roughness? To

522 give some indication of the limitations of the approximation adopted here, we numerically simulate
523 slip on two more complex geometries to quantify how slip is reduced on such surfaces. We have
524 found slip distributions relative to planar faults for 2D and 3D fracture surface geometries observed in
525 the field. The first is from Ritz et al. (2015) and the second an exposed fracture face on a sandstone
526 outcrop reconstructed using 3D photogrammetry. The sampling of this face is such that roughness
527 below a 10th of the half-length is not captured and additional artefacts may have been introduced
528 during processing. Figure 14 also shows approximations of these two fractures with waveforms. For
529 the 2D results for the surface shown in Figure 14 we observe a slip reduction of 17% compared to
530 planar. This compares well to that for the waveform approximation shown, that has an approximate
531 slip reduction of ~12% (Figure 8). For the 3D fracture surface, the slip reduction is 25%. For the
532 approximate waveform from Figure 10 the slip reduction is ~5%. Therefore, for the two surfaces
533 shown here the results suggest that first order approximation will overestimate the volume of slip
534 compared with a natural fracture shape that has multiple length scales of asperities. Intuitively, this
535 will be especially apparent when 3D surface roughness is close to isotropic, i.e. lacking alignment of
536 the asperities. This is seen for small faults (slip < 1 m), which in general are characterised by roughness
537 that is closer to isotropic than larger faults (~10-100 m slip) (Sagy et al., 2007). Power and Dunham
538 (1997) show that roughness on fracture surfaces of both natural and experimental tensile fractures is
539 close to isotropic, at scales of 0.001 to 2 cm. To provide a conflicting example, Pollard et al., (2004)
540 show clear examples of joint surfaces with clear anisotropic roughness perpendicular to the fracture
541 tip lines, on the scale of cm's, formed during mixed mode fracture propagation.

542 In section 1.2 we provide some potential mechanisms that create or cause non-planarity of fractures.
543 None of these mechanisms create the sinusoidal structures observed on some fault surfaces, that are
544 typically above the metre scale (Resor and Meer, 2009; Brodsky et al., 2016). Are our results
545 applicable to such structures? Our model results can be scaled up to a larger scale using the
546 appropriate values in the analytical solutions provided. This is dependent on the assumption that the

547 roughness is not destroyed or modified during slip and that the boundary conditions we have used
548 are still suitable.

549 **6.3 Fluid flow**

550 We have quantified the opening of apertures when wavy fault surfaces shear at fluid pressures close
551 to hydrostatic conditions. These open even when confined by remote stresses driving shearing. This is
552 contrary to the assumption that fluid pressure must exceed the normal stress acting on a fracture
553 face before openings are observed (e.g. Mildren et al., 2002). Figure 13 uses internal pressure as the
554 variable controlling opening of the fracture. To use the data presented in this figure the input
555 pressure must be scaled so there are reasonable values for the remote stresses that drive shearing.
556 Using the elastic parameters and stresses described previously this suggests that a 10 m-long shear
557 fracture with the correct waveform could have had 1.25 cm lenticular openings. It is of interest to
558 know if in a laboratory, an experiment using pre-cut rock samples would also show increases in the
559 permeability during shear loading, for certain cut shapes.

560 **7 Conclusions**

561 We have quantified the amount that slip is reduced by friction on 3D fault surfaces with variations in
562 fault topography. We use a first order approximation where topography is modelled as a sinusoidal
563 waveform, i.e. parallel corrugations. Firstly, when typical friction values are considered the fault plane
564 only slips in directions parallel to the resolved traction vector, independent of its direction in relation
565 to the corrugation alignment. Slip reductions due to corrugations are comparable for both 2D line
566 cracks and 3D penny-shaped cracks when shearing is perpendicular to corrugation alignment.
567 Differences in slip reductions when the slip is aligned and misaligned with corrugations appear to be
568 less than the differences in slip reductions when the corrugation wavelength is doubled, when the
569 out-of-plane stresses are high. When the slip vector is aligned with the corrugations on the fault
570 surface, halving the corrugation wavelength has almost the same effect at reducing slip volume as

571 increasing the out-of-plane stress from close to the lowest stress in the plane of shearing up until it
572 matches the normal stress acting on the plane. For lenticular openings on fault surfaces we have
573 quantified which waveforms have the greatest openings: for typical shearing conditions, this is a λ/H
574 ratio of around 15. Note that opening apertures are observed even when the internal pore fluid
575 pressure does not exceed the remote stresses clamping the fault surface.

576 **8 Acknowledgements**

577 We thank both reviewers for the constructive reviews which resulted in improvements to the
578 manuscript, the editor Cees Passchier and lastly, Lydia Jagger who helped improve the language of
579 the initial draft. The work here was funded through the Deutsche Forschungsgemeinschaft /
580 International Continental Scientific Drilling Program, grant agreement N. RI 2782/3-1.

581 **9 Supplementary material**

- 582 A) MATLAB script containing Eq.(1), (2), (3), (4), (5), (23), (24) and (26). 'AppendixEqs.m'
- 583 B) Text file containing data of triangulation used in numerical analysis. 'Triangulation.csv'

584 **10 References**

- 585 Baydoun, M. and Fries, T.P., 2012. Crack propagation criteria in three dimensions using the XFEM and
586 an explicit–implicit crack description. *International Journal of Fracture*. 178(1-2), 51-70.
- 587 Brodsky, E.E., Kirkpatrick, J.D., Candela, T., 2016. Constraints from fault roughness on the scale-
588 dependent strength of rocks. *Geology*. 44(1), 19-22.
- 589 Bürgmann, R., Pollard, D.D., Martel, S.J., 1994. Slip distributions on faults: effects of stress gradients,
590 inelastic deformation, heterogeneous host-rock stiffness, and fault interaction. *Journal of Structural*
591 *Geology*. 16(12), 1675-1690.

592 Byerlee, J., 1978. Friction of rocks. In *Rock friction and earthquake prediction*. 615-626. Birkhäuser,
593 Basel.

594 Candela, T., Renard, F., Schmittbuhl, J., Bouchon, M., Brodsky, E.E., 2011. Fault slip distribution and
595 fault roughness. *Geophysical Journal International*. 187(2), 959-968.

596 Cann, J.R., Blackman, D.K., Smith, D.K., McAllister, E., Janssen, B., Mello, S., Avgerinos, E., Pascoe, A.R.
597 and Escartin, J., 1997. Corrugated slip surfaces formed at ridge–transform intersections on the Mid-
598 Atlantic Ridge. *Nature*, 385(6614), p.329.

599 Cooke, M.L., Pollard, D.D., 1996. Fracture propagation paths under mixed mode loading within
600 rectangular blocks of polymethyl methacrylate. *Journal of Geophysical Research: Solid Earth*. 101(B2),
601 3387-3400.

602 Choi, M.K., Bobet, A. and Pyrak-Nolte, L.J., 2014. The effect of surface roughness and mixed-mode
603 loading on the stiffness ratio κ_x/κ_z for fractures. *Geophysics*, 79(5), pp.D319-D331.

604 Cowie, P.A., Scholz, C.H., 1992. Physical explanation for the displacement-length relationship of faults
605 using a post-yield fracture mechanics model. *Journal of Structural Geology*. 14(10), 1133-1148.

606 Crider, J.G., 2001. Oblique slip and the geometry of normal-fault linkage: mechanics and a case study
607 from the Basin and Range in Oregon. *Journal of Structural Geology*. 23(12), 1997-2009.

608 Davis, T., Healy, D., Bubeck, A., Walker, R., 2017. Stress concentrations around voids in three
609 dimensions: The roots of failure. *Journal of Structural Geology*. 102, 193-207.

610 Dieterich, J.H., Smith, D.E., 2009. Nonplanar faults: Mechanics of slip and off-fault damage. In
611 *Mechanics, structure and evolution of fault zones*. 1799-1815. Birkhäuser Basel.

612 Dyskin, A.V., Sahouryeh, E., Jewell, R.J., Joer, H. and Ustinov, K.B., 2003. Influence of shape and
613 locations of initial 3-D cracks on their growth in uniaxial compression. *Engineering Fracture*
614 *Mechanics*. 70(15), 2115-2136.

615 Erdogan, F. and Sih, G.C., 1963. On the crack extension in plates under plane loading and transverse
616 shear. *Journal of basic engineering*, 85(4), pp.519-525.

617 Eshelby, J. D. (1963). The distribution of dislocations in an elliptical glide zone. *physica status solidi*,
618 3(11), 2057-2060.

619 Griffith, W.A., Nielsen, S., Di Toro, G. and Smith, S.A., 2010. Rough faults, distributed weakening, and
620 off-fault deformation. *Journal of Geophysical Research: Solid Earth*, 115(B8).

621 Harbord, C.W., Nielsen, S.B., De Paola, N., Holdsworth, R.E., 2017. Earthquake nucleation on rough
622 faults. *Geology*. 45(10), 931-934.

623 Hedayat, A., Pyrak-Nolte, L.J. and Bobet, A., 2014. Multi-modal monitoring of slip along frictional
624 discontinuities. *Rock mechanics and rock engineering*, 47(5), pp.1575-1587.

625 Huang, Y., Yang, Z., Ren, W., Liu, G., Zhang, C., 2015. 3D meso-scale fracture modelling and validation
626 of concrete based on in-situ X-ray computed tomography images using damage plasticity model.
627 *International Journal of Solids and Structures*. 67, 340-352.

628 Janeiro, R.P., Einstein, H.H., 2010. Experimental study of the cracking behaviour of specimens
629 containing inclusions (under uniaxial compression). *International Journal of Fracture*. 164(1), 83-102.

630 Jones, R.R., Kokkalas, S. and McCaffrey, K.J.W., 2009. Quantitative analysis and visualization of
631 nonplanar fault surfaces using terrestrial laser scanning (LIDAR)—The Arkitsa fault, central Greece, as
632 a case study. *Geosphere*, 5(6), pp.465-482.

633 Kattenhorn, S.A., Pollard, D.D., 2001. Integrating 3-D seismic data, field analogs, and mechanical
634 models in the analysis of segmented normal faults in the Wytch Farm oil field, southern England,
635 United Kingdom. *AAPG bulletin*. 85(7), 1183-1210.

636 Kaven, J.O., Hickman, S.H., Davatzes, N.C., Mutlu, O., 2012. Linear complementarity formulation for
637 3D frictional sliding problems. *Computational Geosciences*. 16(3), 613-624.

638 Kim, Y.S., Sanderson, D.J., 2005. The relationship between displacement and length of faults: a review.
639 Earth-Science Reviews. 68(3), 317-334.

640 Kirkpatrick, J.D., Brodsky, E.E., 2014. Slickenside orientations as a record of fault rock rheology. Earth
641 and Planetary Science Letters. 408, 24-34.

642 Li, H., Liu, C.L., Mizuta, Y. and Kayupov, M.A., 2001. Crack edge element of three-dimensional
643 displacement discontinuity method with boundary division into triangular leaf elements.
644 Communications in numerical methods in engineering, 17(6), pp.365-378.

645 Lazarus, V., Buchholz, F.G., Fulland, M. and Wiebesiek, J., 2008. Comparison of predictions by mode II
646 or mode III criteria on crack front twisting in three or four point bending experiments. International
647 Journal of Fracture. 153(2), 141-151.

648 Marshall, S.T., Morris, A.C., 2012. Mechanics, slip behavior, and seismic potential of corrugated dip-
649 slip faults. Journal of Geophysical Research: Solid Earth. 117(B3).

650 Martel, S.J. and Muller, J.R., 2000. A two-dimensional boundary element method for calculating
651 elastic gravitational stresses in slopes. Pure and Applied Geophysics, 157(6-8), pp.989-1007.

652 Meng, C., Maerten, F. and Pollard, D.D., 2013. Modeling mixed-mode fracture propagation in isotropic
653 elastic three dimensional solid. International Journal of Fracture, 179(1-2), pp.45-57.

654 Mildren, S.D., Hillis, R.R., Kaldi, J., 2002. Calibrating predictions of fault seal reactivation in the Timor
655 Sea. The APPEA Journal. 42(1), 187-202.

656 Niebe, S., 2009. Pain and Agony using a Newton Based Method. Masters dissertation, Department of
657 Computer Science, University of Copenhagen, Denmark. Available at:
658 http://image.diku.dk/niebe/niebe_thesis.pdf (Accessed 8 February 2018).

659 Niebe, S., Erleben, K., 2015. Numerical methods for linear complementarity problems in physics-based
660 animation. Synthesis Lectures on Computer Graphics and Animation. 7(1), 1-159.

661 Nikkhoo, M., Walter, T.R., 2015. Triangular dislocation: an analytical, artefact-free solution.
662 Geophysical Journal International. 201(2), 1117-1139.

663 Olson, J. E., 1991. Fracture mechanics analysis of joints and veins. PhD thesis. Stanford University.

664 Olson, J., Pollard, D.D., 1989. Inferring paleostresses from natural fracture patterns: A new method.
665 Geology. 17(4), 345-348.

666 Persson, B.N., 2006. Contact mechanics for randomly rough surfaces. Surface Science Reports. 61(4),
667 201-227.

668 Persson, P.O. and Strang, G., 2004. A simple mesh generator in MATLAB. SIAM review, 46(2), pp.329-
669 345.

670 Pollard, D.D., Bergbauer, S. and Mynatt, I., 2004. Using differential geometry to characterize and
671 analyse the morphology of joints. Geological Society, London, Special Publications, 231(1), pp.153-
672 182.

673 Pollard, D.D., Fletcher, R.C., 2005. Fundamentals of Structural Geology. Cambridge University Press.

674 Pollard, D.D., Segall, P., 1987. Theoretical displacements and stresses near fractures in rock: with
675 applications to faults, joints, veins, dikes, and solution surfaces. Fracture mechanics of rock. 277-349.

676 Power, W.L. and Durham, W.B., 1997. Topography of natural and artificial fractures in granitic rocks:
677 Implications for studies of rock friction and fluid migration. International Journal of Rock Mechanics
678 and Mining Sciences, 34(6), pp.979-989.

679 Renard, F., Mair, K., Gundersen, O., 2012. Surface roughness evolution on experimentally simulated
680 faults. Journal of Structural Geology. 45, 101-112.

681 Resor, P.G., Meer, V.E., 2009. Slip heterogeneity on a corrugated fault. Earth and Planetary Science
682 Letters. 288(3-4), 483-491.

683 Ritz, E., Mutlu, O., Pollard, D.D., 2012. Integrating complementarity into the 2D displacement
684 discontinuity boundary element method to model faults and fractures with frictional contact
685 properties. *Computers & Geosciences*. 45, 304-312.

686 Ritz, E., Pollard, D.D., 2012. Stick, slip, and opening of wavy frictional faults: A numerical approach in
687 two dimensions. *Journal of Geophysical Research: Solid Earth*. 117(B3).

688 Ritz, E., Pollard, D.D., Ferris, M., 2015. The influence of fault geometry on small strike-slip fault
689 mechanics. *Journal of Structural Geology*. 73, 49-63.

690 Roberts, G.P., Ganas, A., 2000. Fault-slip directions in central and southern Greece measured from
691 striated and corrugated fault planes: Comparison with focal mechanism and geodetic data. *Journal of*
692 *Geophysical Research: Solid Earth*. 105(B10), 23443-23462.

693 Sagy, A., Brodsky, E.E. and Axen, G.J., 2007. Evolution of fault-surface roughness with slip. *Geology*,
694 35(3), pp.283-286.

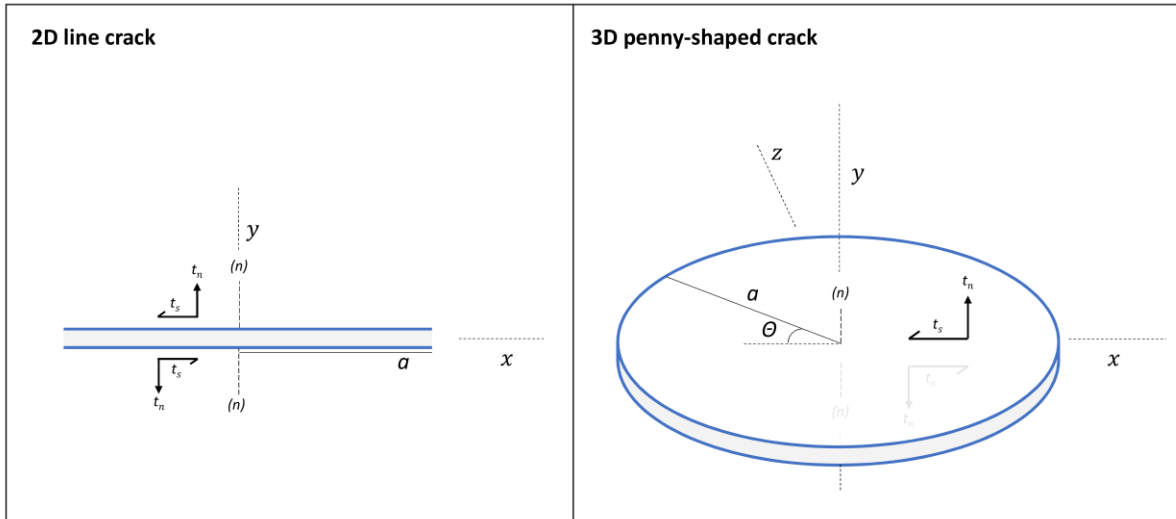
695 Sheibani, F. and Olson, J., 2013. Stress intensity factor determination for three-dimensional crack
696 using the displacement discontinuity method with applications to hydraulic fracture height growth
697 and non-planar propagation paths. In *Effective and Sustainable Hydraulic Fracturing*. InTech.

698 Tada, H., Paris, P.C. and Irwin, G.R., 1973. *The Stress Analysis of Cracks Handbook* 3rd ed. The
699 American Society of Mechanical Engineers.

700 Thomas, A.L., Pollard, D.D., 1993. The geometry of echelon fractures in rock: implications from
701 laboratory and numerical experiments. *Journal of Structural Geology*. 15(3-5), 323-334.

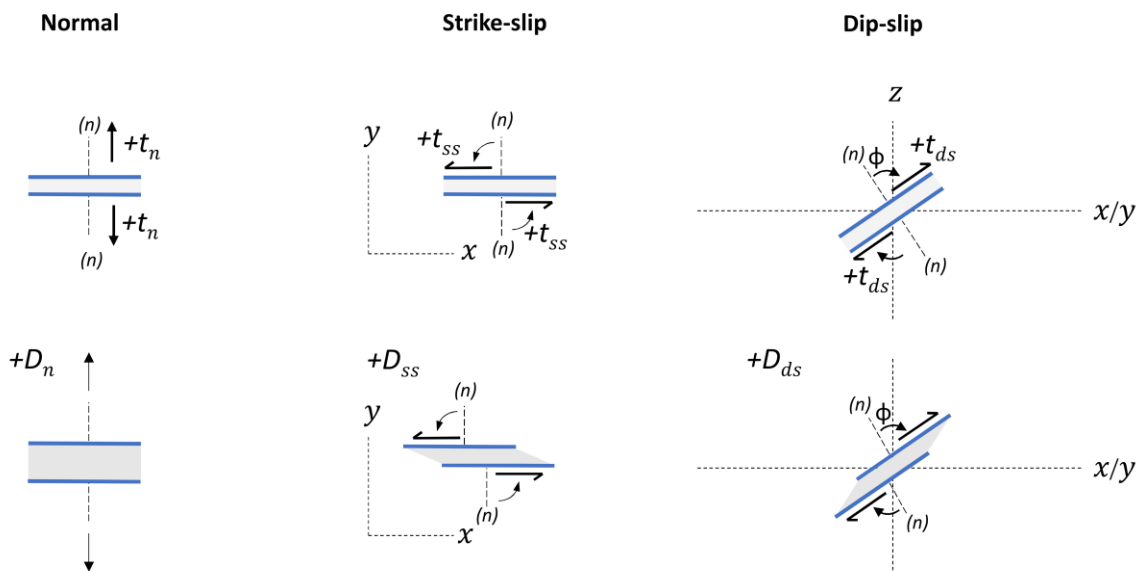
702 Willemse, E.J., 1997. Segmented normal faults: Correspondence between three-dimensional
703 mechanical models and field data. *Journal of Geophysical Research: Solid Earth*. 102(B1), 675-692.

704 **FIGURES**



705

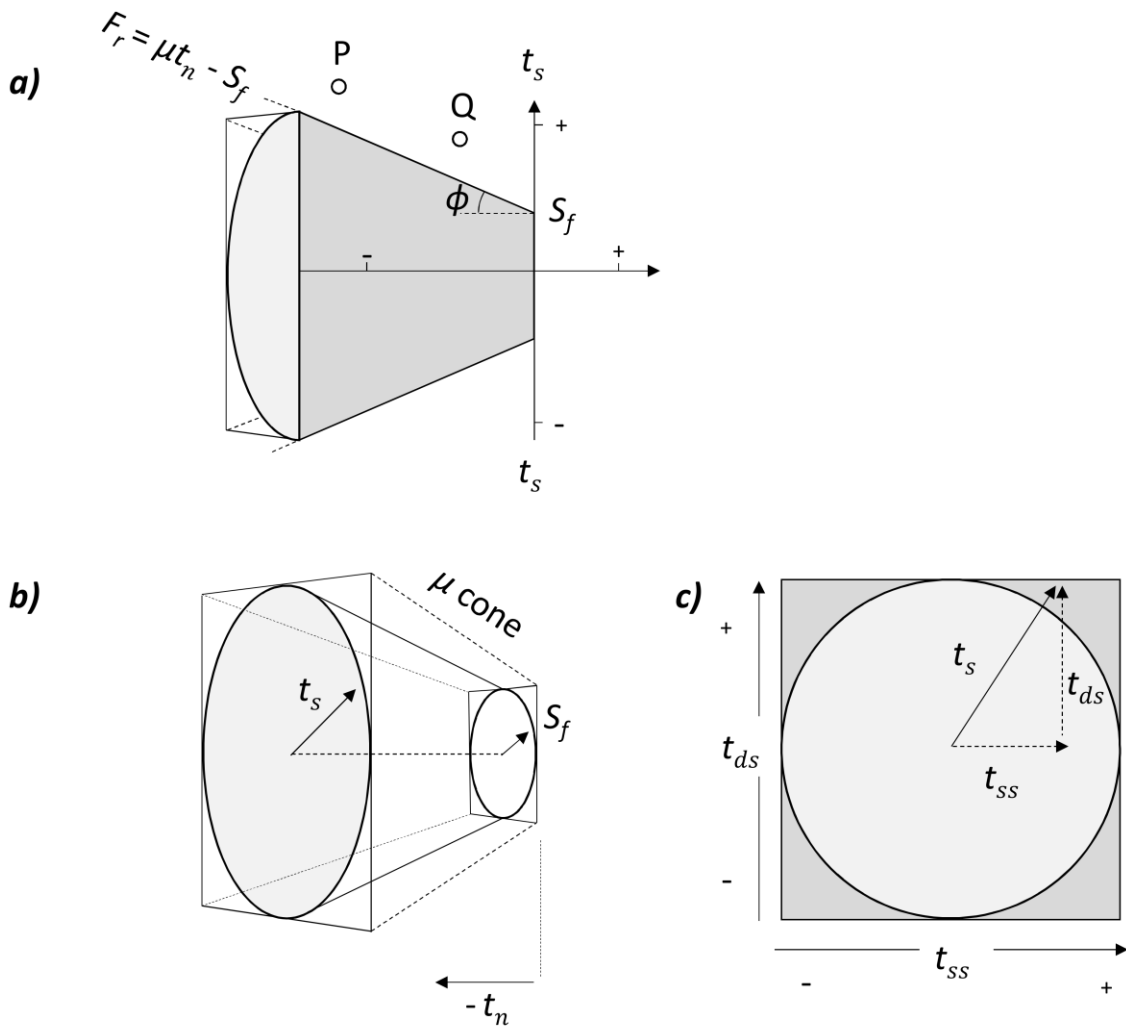
706 Figure 1. Geometry and boundary conditions of the elastic boundary-value problem of a line and
 707 penny-shaped crack subject to uniform shear or tensile loads. Traction directions are relative to the
 708 fractures normal (n) and θ is the angle away from the direction of shearing. The crack surfaces have
 709 been artificially separated (grey area) in order to see its faces and the respective tractions acting on
 710 these.



711

712 Figure 2. Positive displacement and traction component convention adopted for the 3D DDM
 713 formulation. Traction and discontinuity convention match, positive D_n and t_n are opening and tension

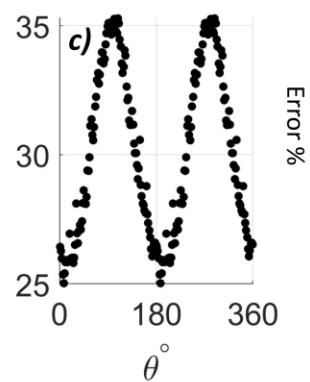
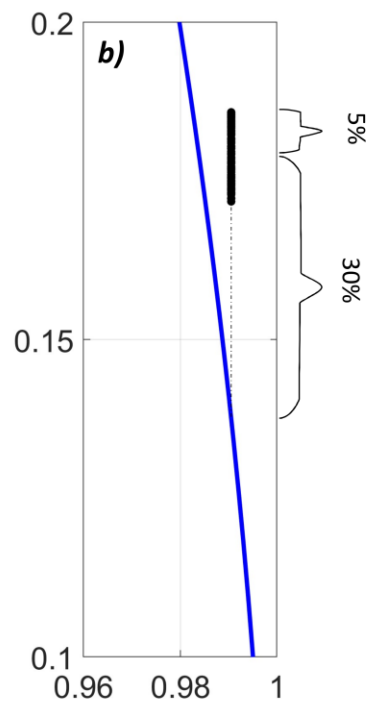
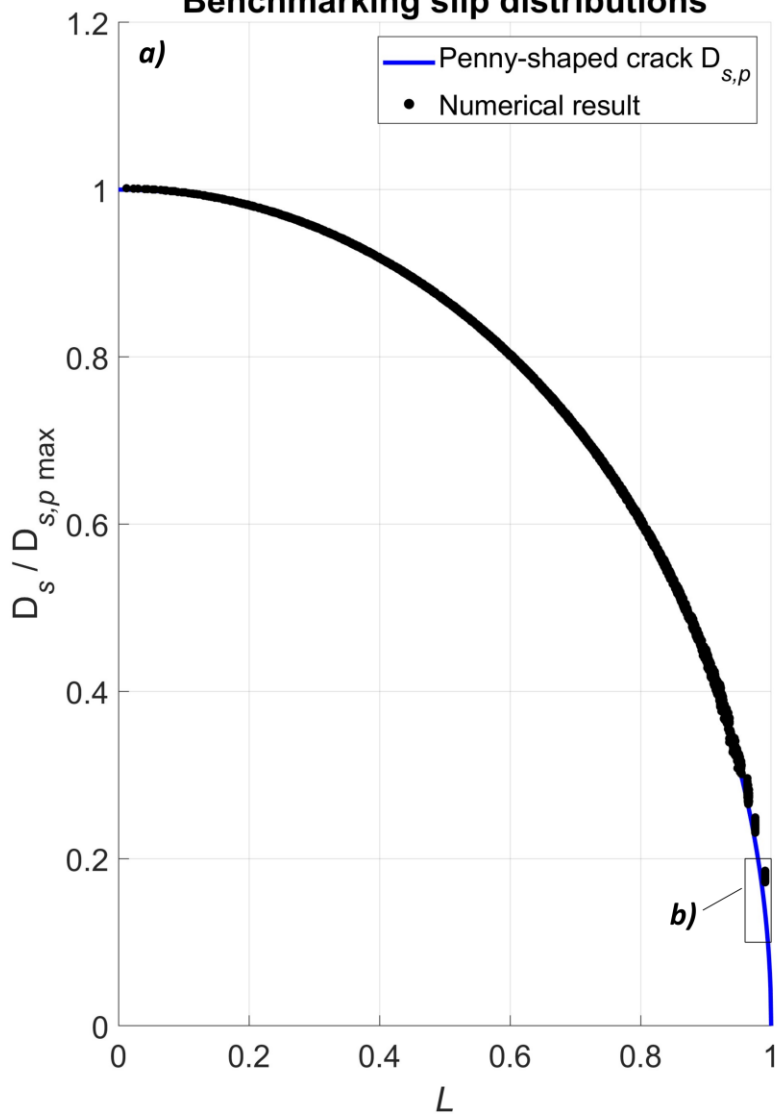
714 respectively. In the xy -plane positive D_{ss} and t_{ss} are left lateral, i.e. along the direction counter-
 715 clockwise from the element normal (n). For D_{ds} and t_{ds} positive directions are those where the angle
 716 between the normal and the shear direction in question (ϕ) contains the z -axis. For flat triangles the
 717 convention of Nikkhoo and Walter (2015) is used, for normal vectors facing upwards, D_{ss} and D_{ds} are
 718 positive when shearing south and west, whereas when the normal vector points downward, positive
 719 directions face north and west.



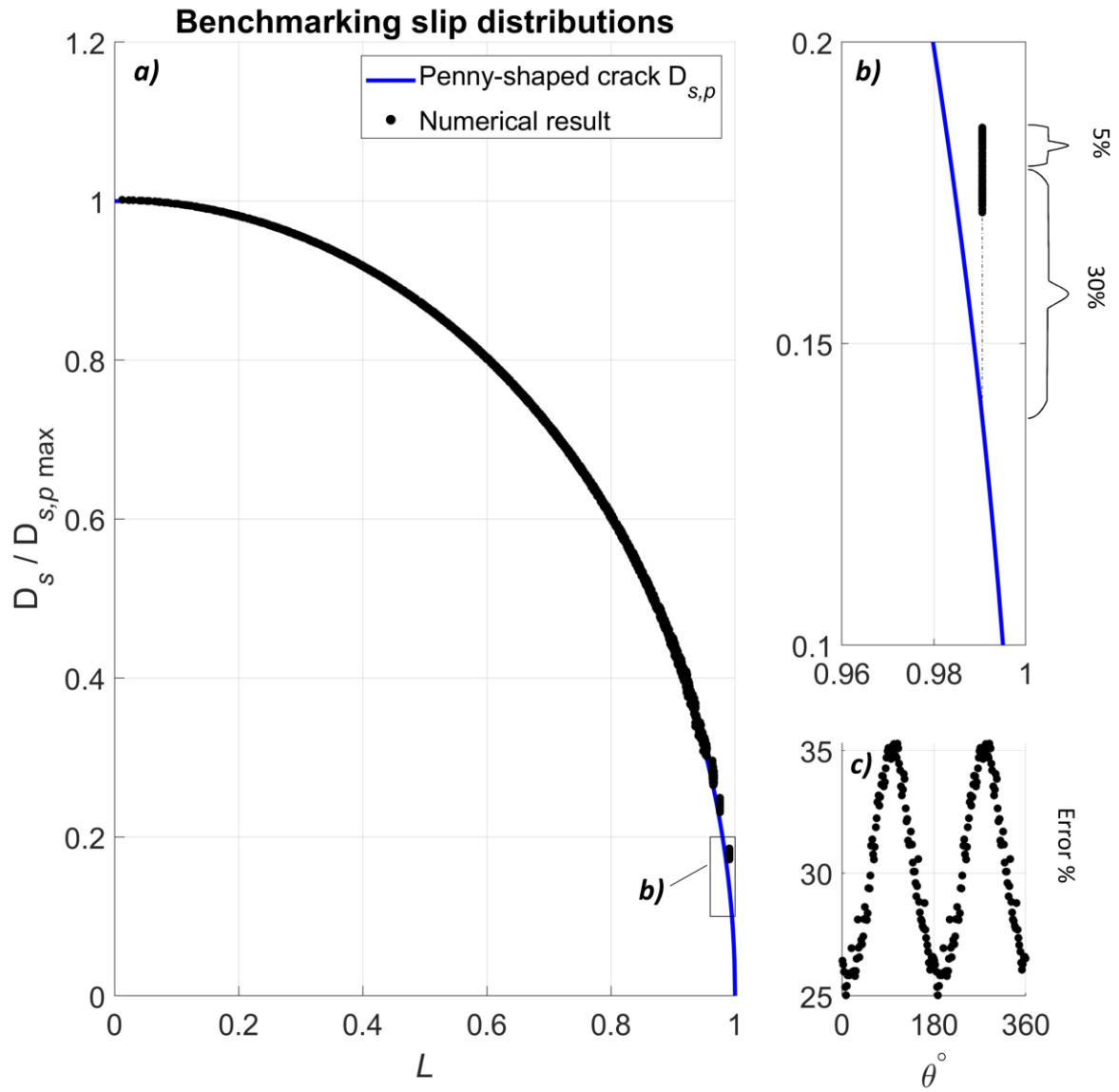
720

721 Figure 3. A summary of the 3D friction cone used in the numerical calculation. Figure adapted from
722 Kaven et al. (2012) & Niebe (2009).

Benchmarking slip distributions

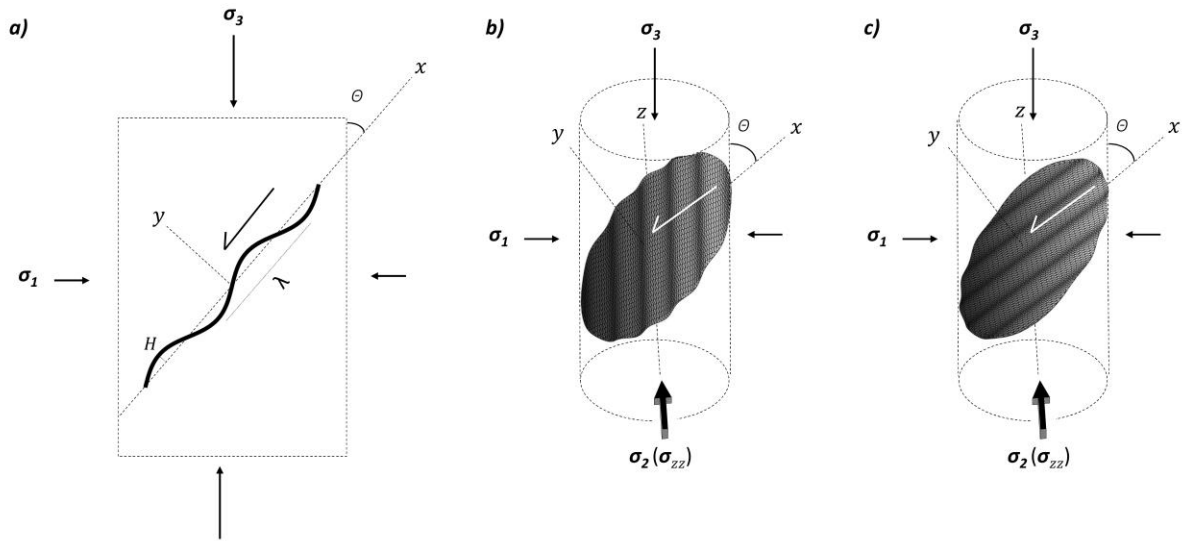


723



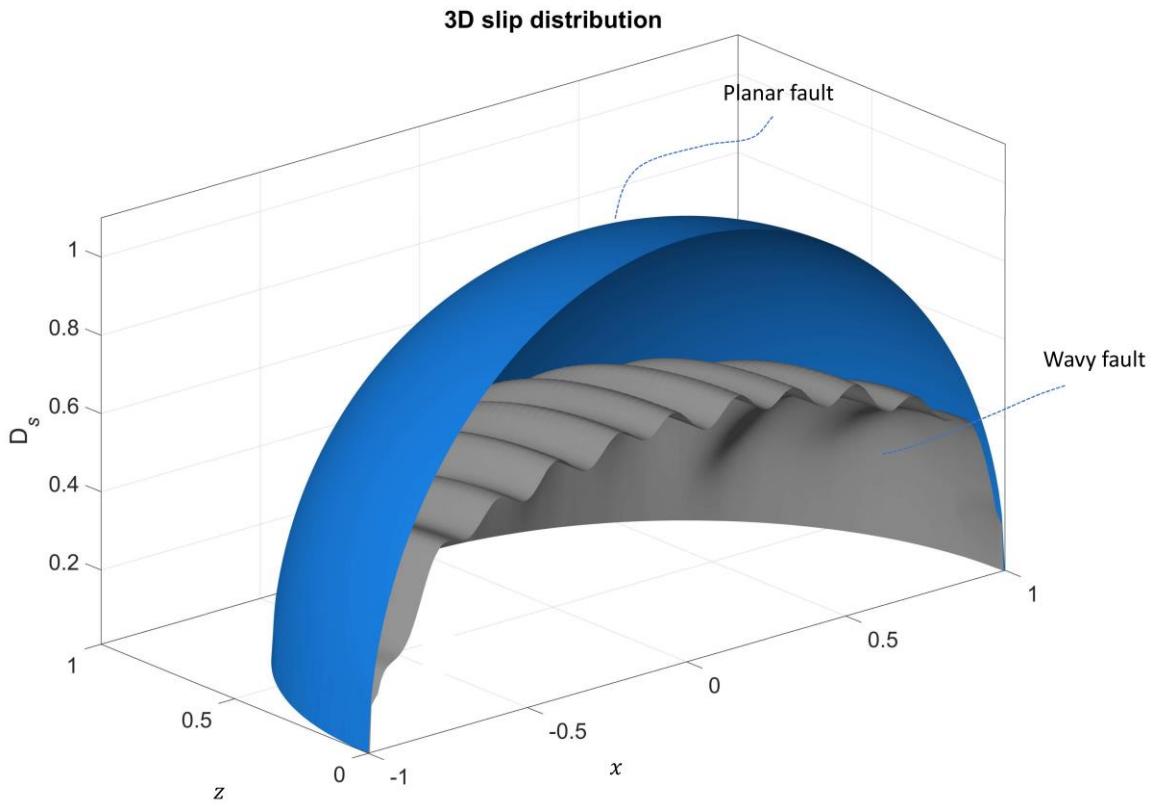
724

725 Figure 4. Benchmarking of the numerical results against analytical solutions. D_s represents the slip of
 726 the penny-shaped crack normalised to the maximum slip value from Eq. (2). The sampling used is
 727 described in the text. c) shows the crack tip elements overestimation of the analytical slip profile in
 728 percent vs θ .



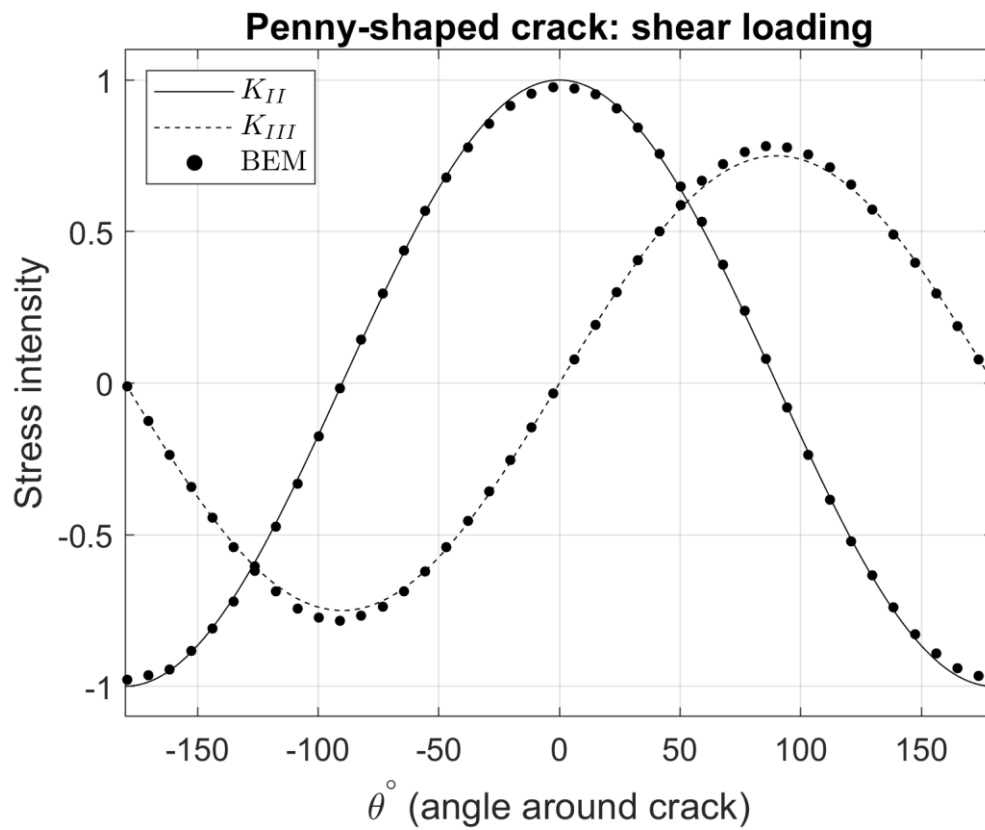
729

730 Figure 5. a) Boundary conditions used in the numerical analysis that lie in the xy -plane. λ is the
 731 wavelength and the amplitude is H . b) Slip direction (white arrow) perpendicular corrugations. c) Slip
 732 direction parallel with corrugations. Note that the dashed boundaries are included to highlight the
 733 principal stress directions, the fracture surfaces modelled lie within an infinite elastic medium.

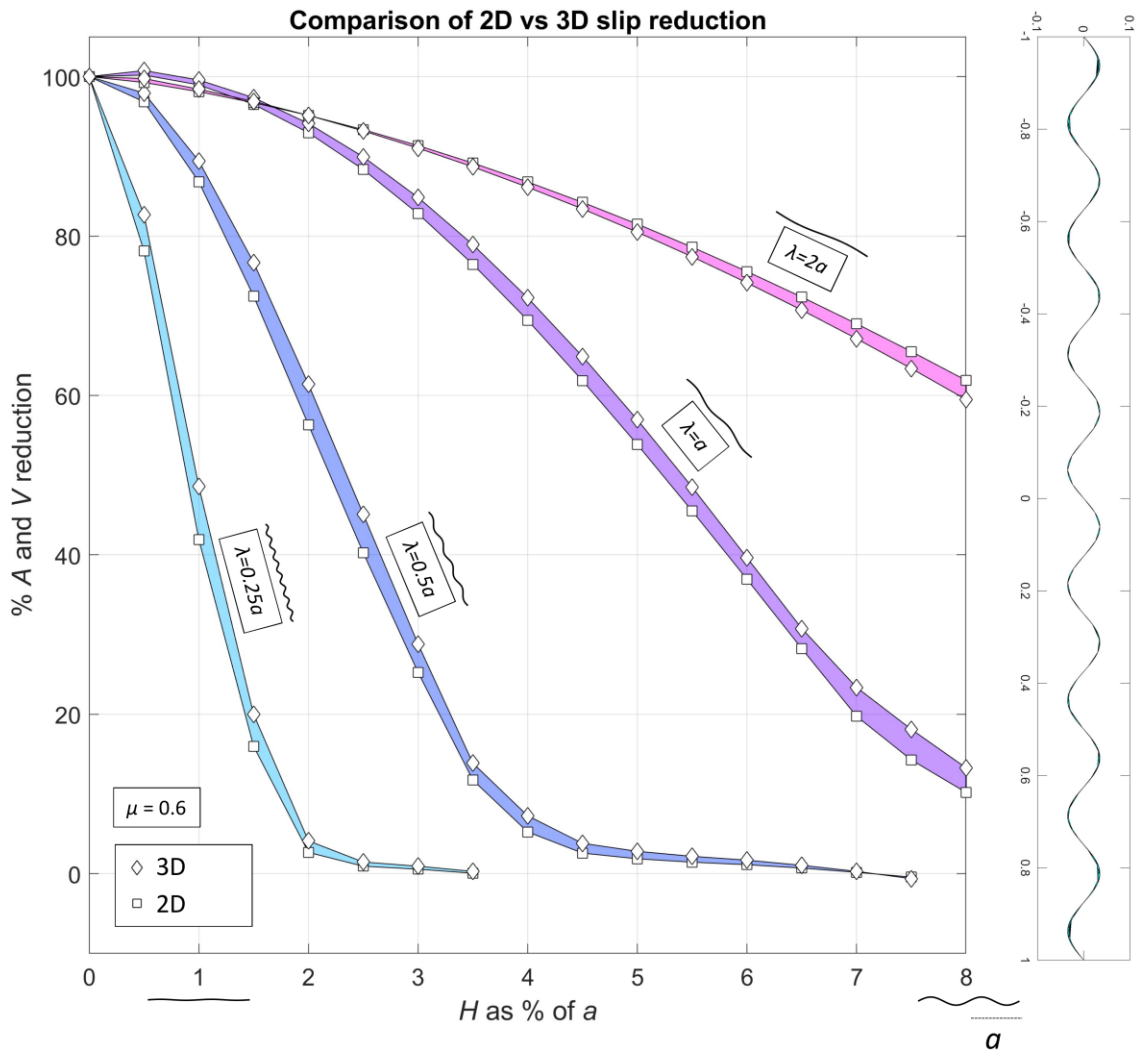


734

735 Figure 6. Cross section through 3D slip distributions for a planar and wavy fault. Here $a=1$ and the xz
 736 axes of the graph are the location on the cracks walls. The wavy fault has an H and λ that are 2% and
 737 37.5% of a respectively. Driven by the boundary conditions described in Section 4. D_s here is slip
 738 normalised to a planar faults maximum slip value from Eq. (2).



739
 740 Figure 7. Stress intensity factor approximation using the 3D DDM method. Analytical curves shown
 741 are for a penny-shaped crack subject to shear stress; Eq. (24). All results are normalised the maximum
 742 analytical value of K_{II} . The numerical approximation is shown as dots. The sampling used, and
 743 boundary conditions on the fracture are those described in Section 4.1. The signs here follow the
 744 shear direction convention shown in Figure 9.30 of Pollard and Fletcher (2005). The positive direction
 745 of the crack y -axis in Figure 5b corresponds to the y -axis in the local coordinate system of their figure.



746

747 Figure 8. Comparison between numerical results for 2D (A) and 3D (V) slip reduction due to changes

748 in a wavy fault surfaces amplitude and wavelength. Squares are the resultant 2D slip area and

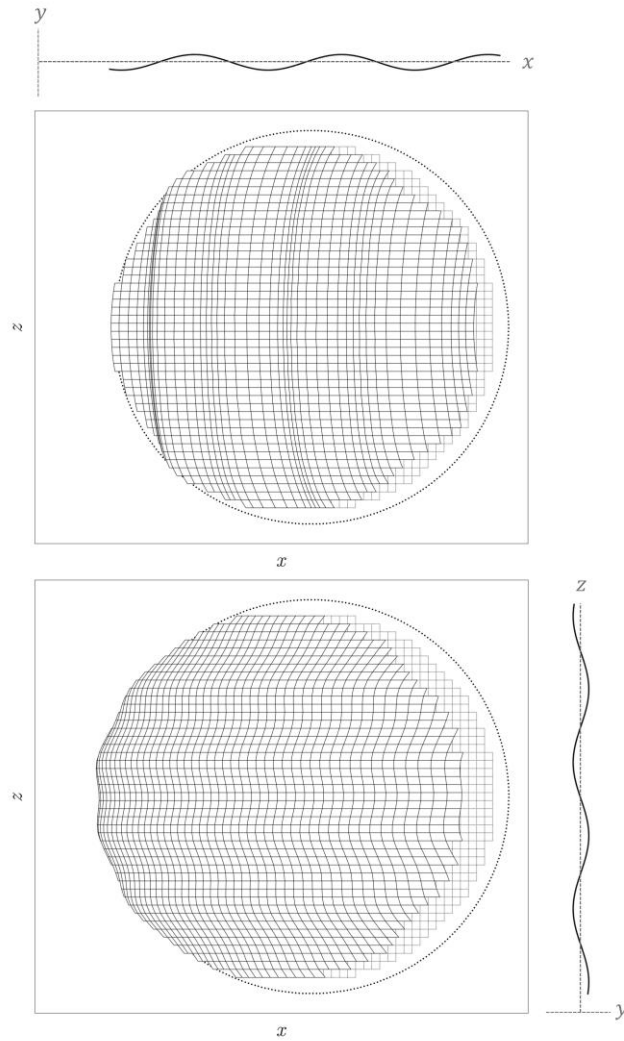
749 diamonds are the 3D slip volume. Results on the y-axis are relative to Eqs. (3) & (4). Different colours

750 on the graph correspond to different wavelengths relative to half-length a . On the right of the figure

751 we show our mesh captures the most extreme waveform we show this looking down the corrugations

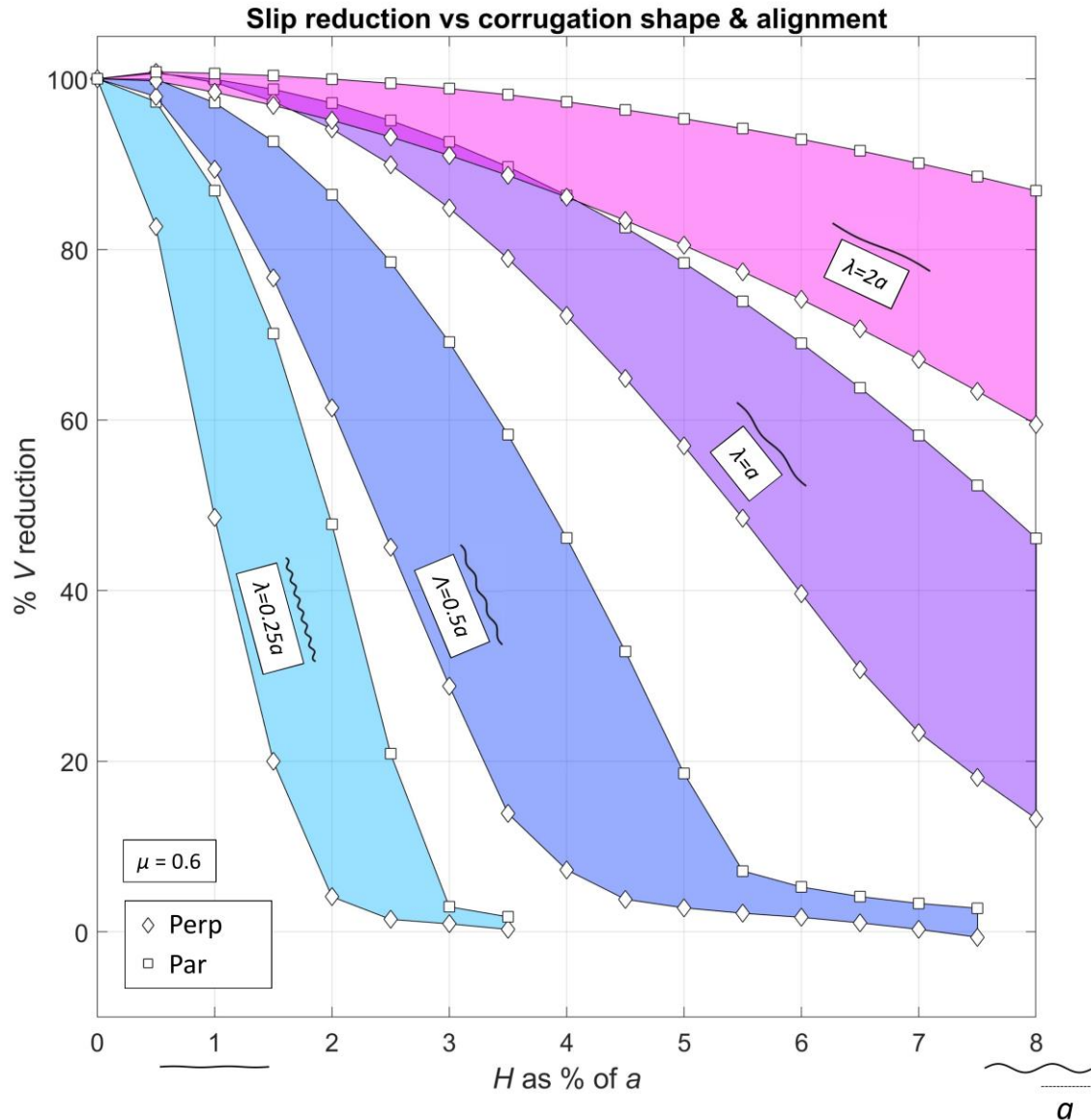
752 for a waveform where H and λ are 3.5% and 25% of a respectively. The slight deviations at the wave

753 crests are caused by the added equilateral edge triangles.



754

755 Figure 9. Deformation pattern of the fracture walls when slip is perpendicular (top) and parallel
 756 (bottom) to corrugations. The dotted line represents the fractures boundary. The light uniformly
 757 gridded squares in the background represent one of the fracture walls before deformation. The
 758 deformed grid is the resultant displacement once this wall shears. The topography of the surface is
 759 shown as the 2D lines at the side; this waveform corresponds to an H and λ that are 4% and 75% of a
 760 respectively. Boundary conditions are those as stated in Section 4.1 but the displacement is
 761 exaggerated by 300 times. xz axes correspond to those shown in Figure 5b) and c). σ_{zz} here has been
 762 set equal to σ_{xx} .

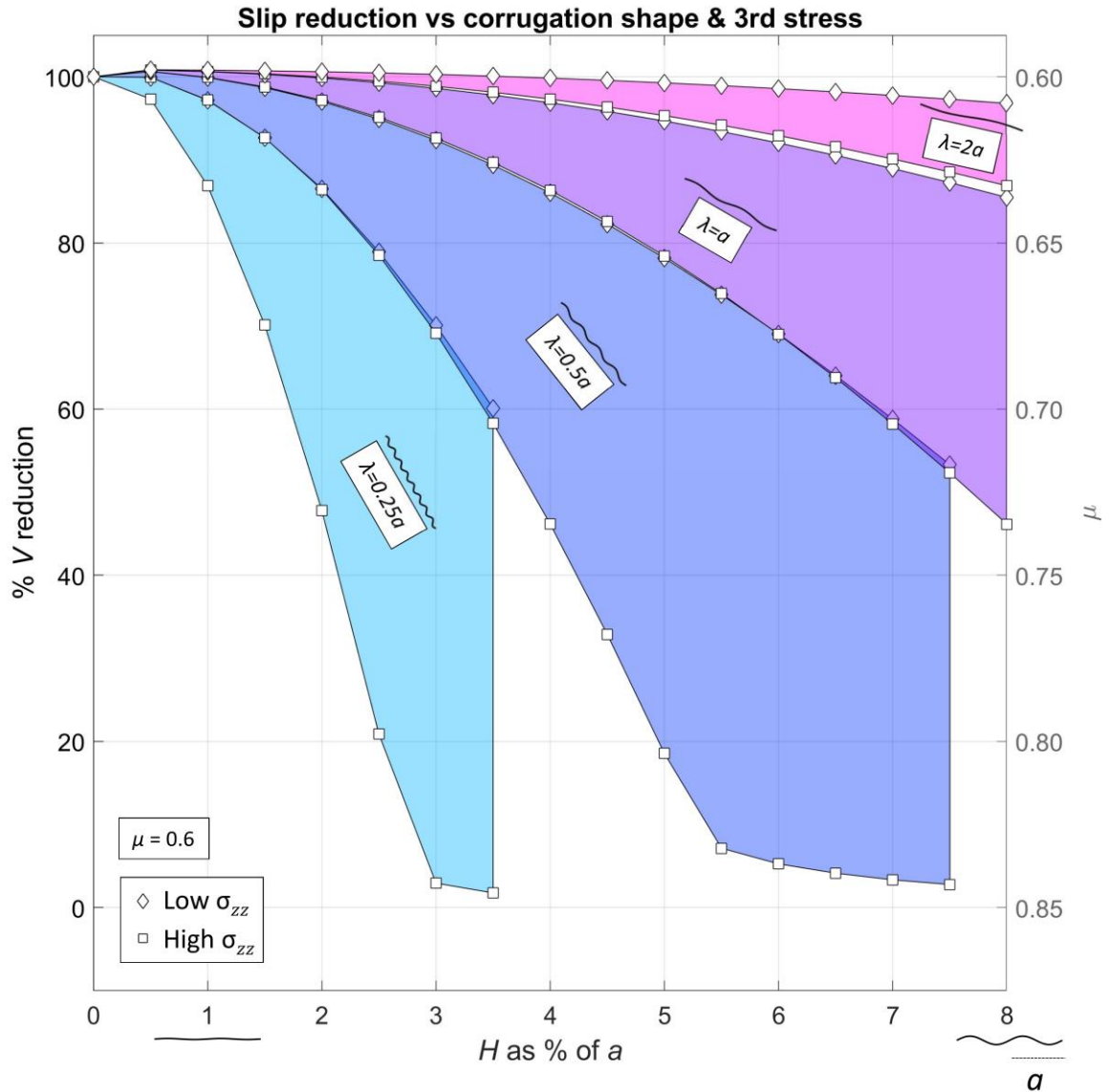


763

764 Figure 10. 3D slip V reduction due to changes in a wavy fault surfaces amplitude and wavelength.

765 Diamonds are when slip is perpendicular with corrugations and squares parallel. Note perpendicular
 766 results match those in Figure 8. Results on the y - axis are relative to a planar fault described by Eq.

767 (4). Different colours on the graph correspond to different wavelengths relative to half-length a .



768

769 Figure 11. 3D slip V reduction due to changes in a wavy fault surfaces amplitude and wavelength.

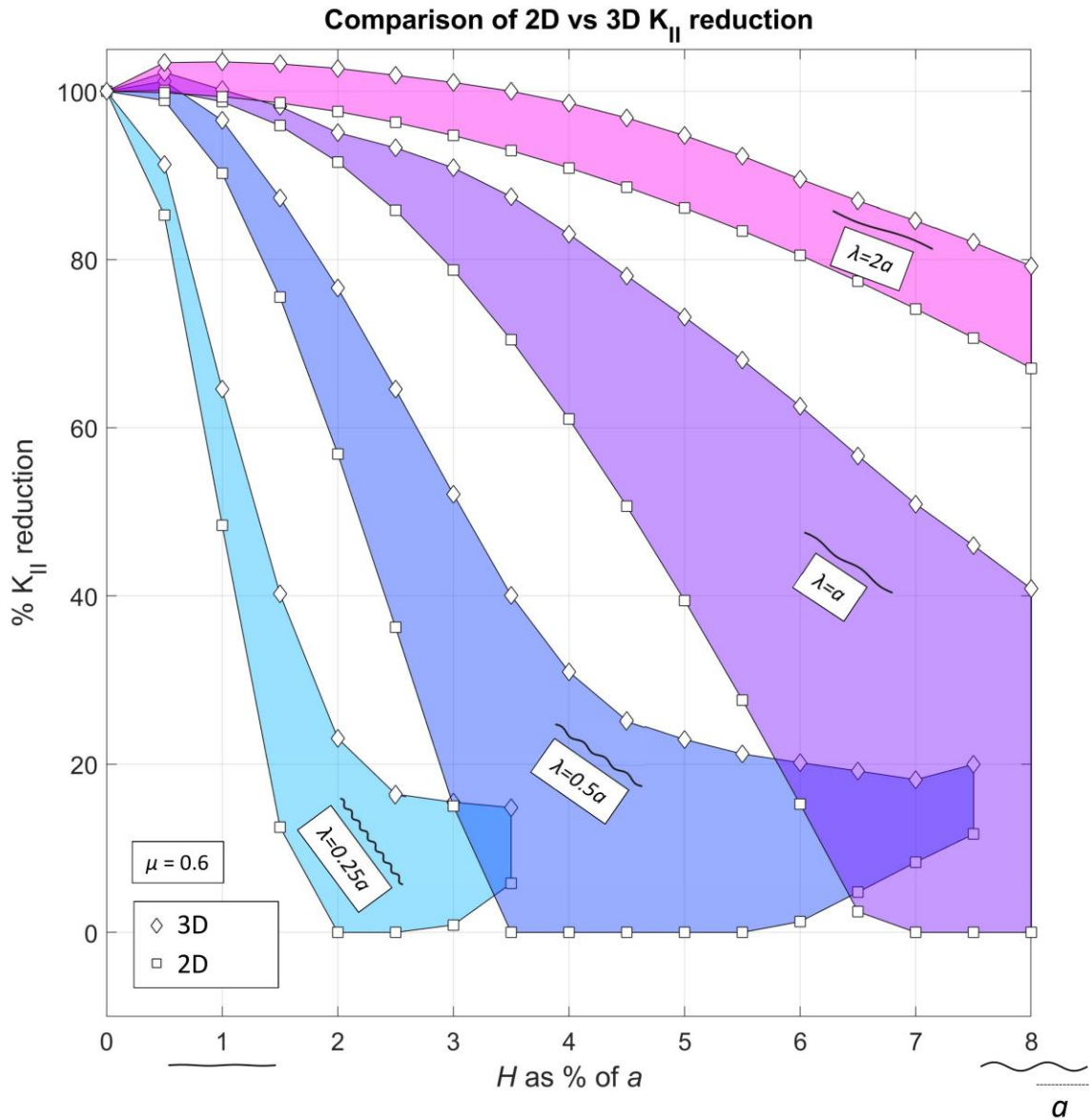
770 Diamonds are when the stress out of the plane of shearing is low (equal to σ_{yy}) and squares when this

771 is high (equal to σ_{xx}). Results on the y - axis are relative to a planar fault described by Eq. (4). Different

772 colours on the graph correspond to different wavelengths relative to half-length a . Values of μ shown

773 on the right of y -axis are adjusted coefficients of friction for planar faults, these will reduce the slip

774 volume by the amount shown on the left y -axis (relative to the volume when μ is 0.6).

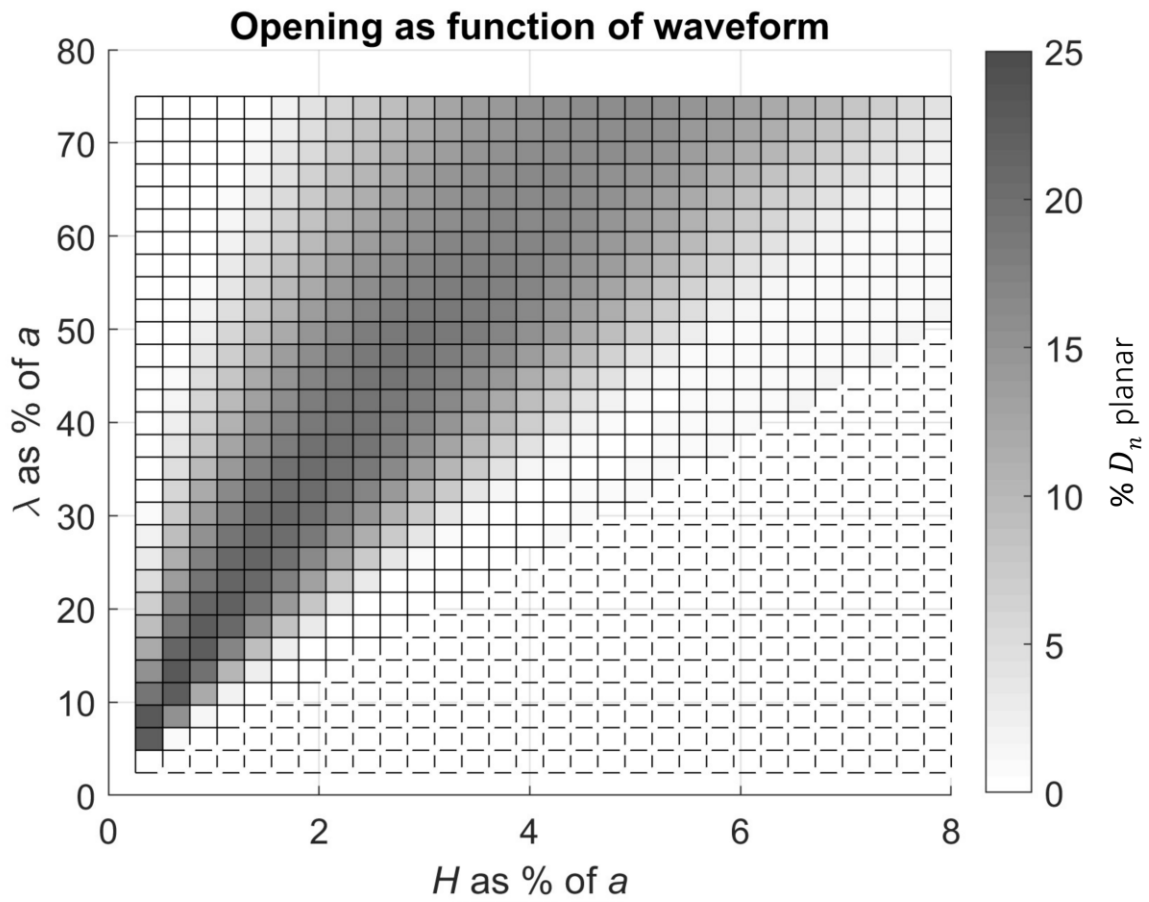


775

776 Figure 12. Stress intensity factor reductions due to corrugations, comparison between 2D and 3D

777 results. Results on the y - axis are relative to a planar fault described by Eq.(24). Different colours on

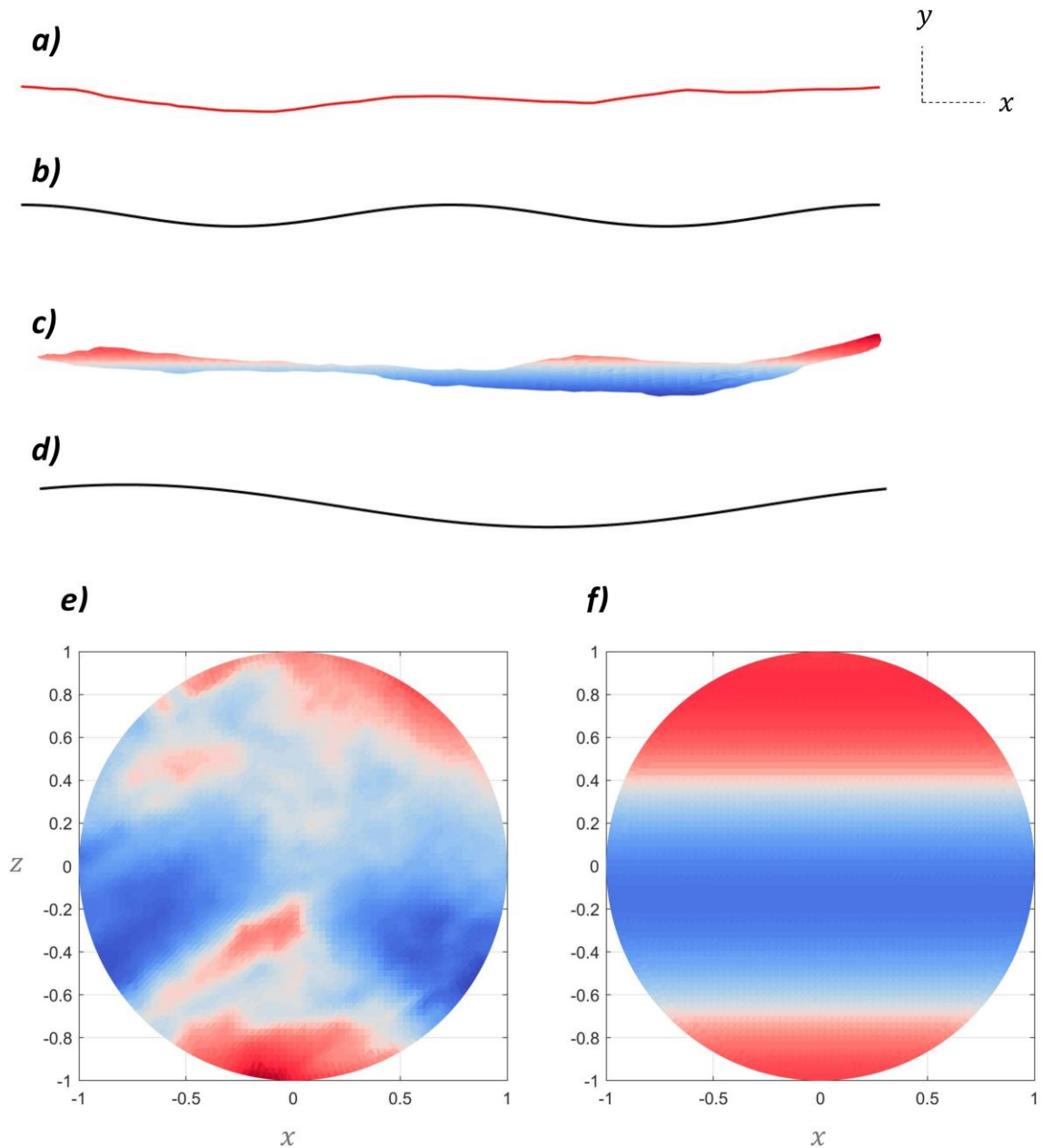
778 the graph correspond to different wavelengths relative to half-length a .



779

780 Figure 13. Waveform and associated lenticular opening apertures on the fault surface. Results scaled

781 relative to Eq. (26).



782

783 Figure 14. a) 2D fracture profile from Ritz et al. (2015), Figure 8, fracture is approximately 3m long. b)

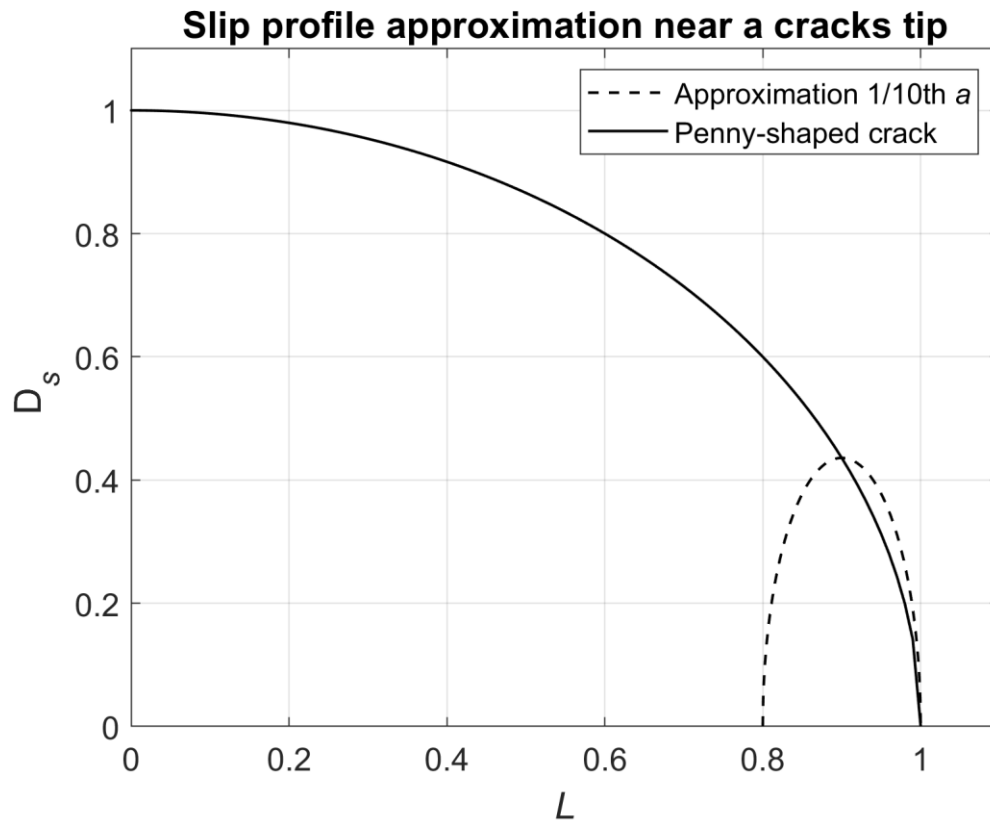
784 2D approximation with waveform: $\lambda = a$, $H = 2.5\%$ of a . c) 3D fracture surface from photogrammetry

785 on a sandstone block (self-defined edges), the exposed fracture surface was 2m wide, looking into the

786 x -axis (slip direction). The height of the surface in the y -axis varies by 14cm. d) Approximation of c)

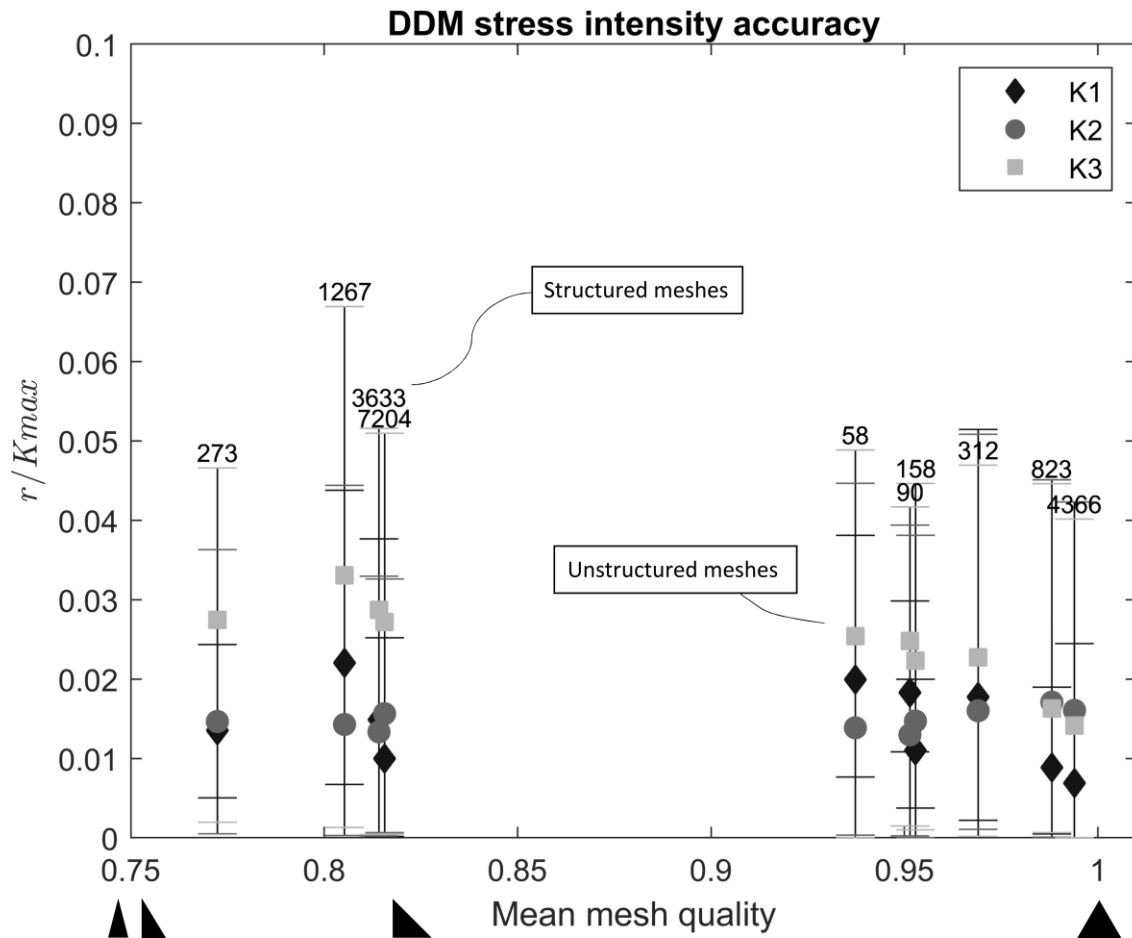
787 with the waveform: $\lambda = 200\%$ of a , $H = 5\%$ of a . e) 3D fracture surface front coloured for height/depth

788 away from 0. f) 3D fracture surface front approximation of d) with the same colour scale as e).



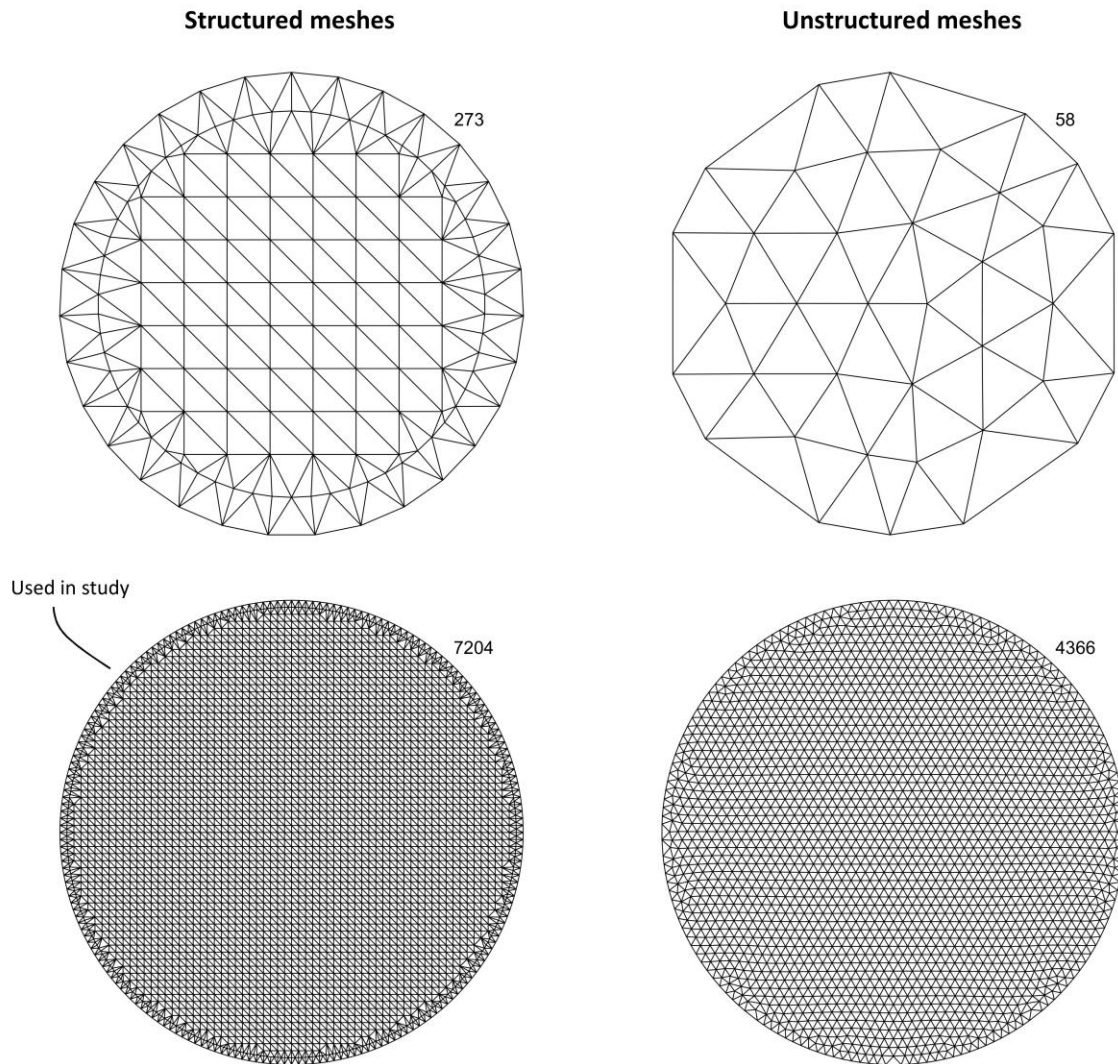
789

790 Figure 15. Comparison between crack wall displacements for a penny-shaped crack and an
 791 approximation of displacements close to the tip for a fracture a 10th of the length.



792

793 Figure 16. The resulting stress intensity error for multiple meshes, compared to analytical solutions
 794 for an inclined penny shaped crack subject to tension. ν was set to 0.25 for all runs. The maximum and
 795 minimum errors are shown as solid horizontal lines, mean as shapes. Shades highlight the mode. The
 796 mean error shown in the y -axis is the sum of residuals r divided by the number of edge triangles n
 797 divided by the maximum value of the stress intensity in question for this geometry. The x -axis shows
 798 the mean mesh quality, defined as two times the radius of the triangles inscribed circle to the radius
 799 of its circumscribed circle. A value of one is a mesh where all triangles are equilateral, some examples
 800 triangles are shown below their respective values. Mesh sizes (number of triangles) are shown above
 801 each data point.



802
 803 Figure 17. The lowest and highest density meshes used in Figure 16. The text describes the number of
 804 triangles. The mesh used in the bottom left is the mesh used in this study as described in Section 4.1.

805 **11 Appendix A**

806 The aim of this section is to detail how we derive the equations for the stress intensity approximation
 807 using the 3D displacement discontinuity method. This allows us to provide reasons for the error in the
 808 equation and propose a value to correct for this. We then go on to detail the errors for different
 809 meshes types and refinements.

810 It is of note to add that other formulations exist for approximating stresses at a cracks tips using the
 811 BEM DDM method, these are either directly calculating stress distributions around the tip or using

812 more complex discontinuities on the crack edge (Meng et al., 2013; Li et al., 2001). The method of
813 Meng et al. (2013) lacks propagation criterion that are related to measurable fracture strengths of
814 materials but could be adapted for this, the method of Li et al. (2001) directly calculates K_I but has
815 does not detail how to work with shear fractures. Sheibani and Olson (2013) describe a similar
816 method to described here for rectangular dislocation elements in 3D, we go into greater detail,
817 deriving the formulas in 3D to show these are the same as 2D, this derivation allows us to correctly
818 identify the sources of error and appropriately adjust for these. We then quantify the accuracy of our
819 approximation.

820 Tada et al., (1973) supply stress intensity factors for 3D penny-shaped cracks loaded by remote
821 stresses:

$$K_I = 2t_n\sqrt{a/\pi} \quad (27)$$

$$\begin{Bmatrix} K_{II} \\ K_{III} \end{Bmatrix} = \begin{Bmatrix} \cos \theta \\ \sin \theta (1 - \nu) \end{Bmatrix} \frac{4t_s\sqrt{a/\pi}}{2 - \nu} \quad (28)$$

822 And Eshelby (1963) gives the separation distance between the walls of the crack (penny):

$$D_n = \frac{4a(1 - \nu)t_n}{\pi G} \sqrt{1 - \frac{L^2}{a^2}} \quad (29)$$

$$D_s = \frac{8(1 - \nu)at_s}{\pi(2 - \nu)G} \sqrt{1 - \frac{L^2}{a^2}} \quad (30)$$

823 Rearranging these to give this in terms of traction:

$$D_n \frac{1}{\sqrt{1 - \frac{L^2}{a^2}}} * \frac{\pi G}{4a(1 - \nu)} = t_n \quad (31)$$

$$D_s \frac{1}{\sqrt{1 - \frac{L^2}{a^2}}} * \frac{\pi(2 - \nu)G}{8(1 - \nu)a} = t_s \quad (32)$$

824 Combining Eq. (27)(28) with (31)(32), note D_{III} the displacement vector parallel to the crack edge and
825 D_{II} is perpendicular to this, in the plane of the crack. This removes the dependence on θ in Eq. (28).

$$K_I = D_n \frac{1}{\sqrt{1 - \frac{L^2}{a^2}}} * \frac{2\sqrt{a/\pi} \pi G}{4a(1 - \nu)} \quad (33)$$

$$\begin{Bmatrix} K_{II} \\ K_{III} \end{Bmatrix} = \begin{Bmatrix} D_{II} \\ D_{III}(1 - \nu) \end{Bmatrix} \frac{1}{\sqrt{1 - \frac{L^2}{a^2}}} * \frac{4\sqrt{a/\pi} \pi(2 - \nu)G}{(2 - \nu)8(1 - \nu)a} \quad (34)$$

826 As the crack tip is approached the reciprocal term goes to zero. Assuming sufficient sampling of the
827 crack so the edge elements are close to the tip we therefore drop this term.

$$K_I = D_n \frac{2\sqrt{a/\pi} \pi G}{4a(1 - \nu)} \quad (35)$$

$$\begin{Bmatrix} K_{II} \\ K_{III} \end{Bmatrix} = \begin{Bmatrix} D_{II} \\ D_{III}(1 - \nu) \end{Bmatrix} \frac{4\sqrt{a/\pi} \pi(2 - \nu)G}{(2 - \nu)8(1 - \nu)a} \quad (36)$$

828 After some rearrangement:

$$\begin{Bmatrix} K_I \\ K_{II} \\ K_{III} \end{Bmatrix} = \begin{Bmatrix} D_n \\ D_{II} \\ D_{III}(1 - \nu) \end{Bmatrix} \frac{\sqrt{a}\sqrt{\pi}G}{a(1 - \nu)2} \quad (37)$$

829 As $\sqrt{x}/x=1/\sqrt{x}$ then:

$$\begin{Bmatrix} K_I \\ K_{II} \\ K_{III} \end{Bmatrix} = \begin{Bmatrix} D_n \\ D_{II} \\ D_{III}(1 - \nu) \end{Bmatrix} \frac{\sqrt{\pi}G}{\sqrt{a}(1 - \nu)2} \quad (38)$$

830 The BEM DDM method supplies displacements on the crack wall. If h is substituted for a in Eq.(38) we
831 simulate a smaller crack with the same opening as the crack tip element close to the fractures tip.
832 Such a crack will have a similar opening profile very close to the tip, i.e. Figure 15 and therefore a
833 similar stress intensity. This approximation means the terms that specify the crack size in the
834 equations is dropped. Constant c is also added which can be used to correct for the mismatch
835 between the approximation and the analytical solution.

$$\begin{Bmatrix} K_I \\ K_{II} \\ K_{III} \end{Bmatrix} = \begin{Bmatrix} D_n \\ D_{II} \\ D_{III}(1 - \nu) \end{Bmatrix} \frac{\sqrt{\pi}G}{\sqrt{h}(1 - \nu)2} c \quad (39)$$

836

837 **Figure 15 here**

838 The correction factor c therefore adjusts for error in the approximation detailed above, the fact we
839 drop the reciprocal term when deriving the equations, and that due to the overestimation of crack
840 wall displacements from the BEM-DDM method. Figure 4 shows that the error due to the
841 overestimation of crack wall displacements is $\sim 30\% \pm 5\%$, this error is similar for opening
842 displacements. This overestimation is close to being independent of mesh refinement which can be
843 seen when we compute the accuracy of the approximation. Using analytical formulas, we compute
844 one source of error. Comparing stress intensities for cracks under the same boundary conditions
845 between a crack where $a=1$ using Eqs. (27) & (28) to the results of Eq. (39) using a displacement of a
846 crack where a is a 1000th of the width with its max displacement defined by the crack wall
847 displacement of the larger crack (Eqs. (29) & (30)). The overestimation of the approximation of Eq.
848 (39) is 41.4%. Combining the two errors the total error of the numerical method is 183.4%. The
849 correction factor is therefore simply $1/1.834$.

850 **Figure 16 here**

851 **Figure 17 here**

852 Figure 16 shows the error due to the stress intensity approximation described, this is compared to the
853 analytical formula for an inclined crack subject to tension described in Tada et al., (1973). We have
854 tested different crack geometries: with normals between 5 and 85 degrees away from z , and the
855 errors for each angle are coincident provided the mesh is the same. The figure shows the results of
856 different meshes, triangulated uniform grids (with an edge of equilateral triangles added) like used in
857 this study and unstructured meshes from the code DistMesh (Persson and Strang, 2004). Note that
858 for both cases we have set a constraint that all the edge triangles are isosceles, see Figure 17 for
859 examples. The results show the error is relatively stable, with the mean values (shapes) below 4% of
860 the maximum analytical value of each stress intensity. Structured meshes appear to have slightly

861 higher errors, even though for these meshes we have put equilateral triangles around the crack edge.
862 The scatter in the crack tip error as shown in Figure 4 must therefore be larger for such meshes. For
863 the unstructured meshes the number of triangles (numbers above each data point) increases mean
864 mesh quality, there is a trend for K_{II} and K_{III} where mesh density increases the mean accuracy, but
865 the error is only halved as the mesh size is squared. It must be noted that ν changes the scatter of the
866 crack tip element slip distribution error in shown in Figure 4. This only affects the slip profile
867 estimation of the DDM, for opening this scatter is constant, around 3% for the mesh used in our
868 analysis. For a ν of 0.01 the shear component scatter drops from around 5% to 2% and when
869 increased to 0.49 it is close to 10%. These errors are for the mesh we have used in the rest of the
870 analysis. This change in the scatter with ν in turn affects the error of the stress intensity
871 approximation of K_{II} and K_{III} .

872 In this section we have detailed a method to approximate stress intensities at a fractures tip in 3D
873 where the fracture can have frictional constraints. The method to calculate stress intensities is simple
874 to implement in BEM DDM formulations or in other methods provided the crack opening/slip profile
875 can be estimated. After correcting for the error of the approximation we have described the error in
876 the stress intensities from using this method. This is caused by scatter in the methods estimation of
877 crack tip displacements. Methods to improve the consistency of the crack opening/slip profile near to
878 the tips have potential to reduce this error.

879 **12 Appendix B**

880 MATLAB scripts containing the DDM code used in this research can be found at:

881 <https://github.com/Timmmdavis/CutAndDisplace>